Impedance Modeling for Three-Phase Inverters with Double Synchronous Reference Frame Current Controller in the Presence of Imbalance

Beloqui Larumbe, Lucia; Qin, Zian; Wang, Lu; Bauer, Pavol

DOI
10.1109/TPEL.2021.3107045

Publication date
2021

Document Version
Accepted author manuscript

Published in
IEEE Transactions on Power Electronics

Impedance Modelling for Three-Phase Inverters with Double Synchronous Reference Frame Current Controller in the Presence of Imbalance

Lucia Beloqui Larumbe, *Student Member, IEEE,* Zian Qin, *Senior Member, IEEE,* Lu Wang, *Student Member, IEEE,* and Pavol Bauer, *Senior Member, IEEE*

***Abstract*—This paper presents a small-signal model for power-electronics converters that use a typical control structure in wind energy applications: the double Synchronous Reference Frame (SRF) current control. The paper considers the presence of unbalanced currents and voltages, and analyses their impact on the frequency couplings of the converter. In addition, it is revealed that, in the presence of negative-sequence voltage synchronization, the converter presents an additional coupling at $-2f_1 - f_\mathbf{p}$.**

***Index Terms*—Double Synchronous Reference frame, small-signal modelling, impedance modelling, frequency coupling, phase locked loop (PLL)**

I. Introduction

With the rise of renewable energies, distributed-power generation, microgrids and other applications, the penetration of power-electronic converters (PECs) has notably increased in recent years. As a result, PECs have a growing impact on the power quality and stability of power systems [1], having caused several incidents as reported in [2]–[5].

In this context, small-signal models of converters and, in particular, impedance models of converters [6]–[11], have been proven to be a useful tool for system-wide stability [12], [13], power quality [14] and resonance studies [15], [16]. However, when modelling converters, most of the literature assumes a balanced grid (e.g. [6]–[8]). Under this assumption, despite being a time-variant AC system, it is possible to find a time-invariant operating point if the equations are taken to the dq frame, where traditional linearization can be undertaken [6]. Nevertheless, when the grid is unbalanced, this is not possible, since the negative-sequence voltage introduces a component at 100 Hz in the positive-sequence dq frame. In other words, there is no single reference frame in which the signals remain constant [17].

This posses a challenge when linearizing the converter. This paper belongs to a growing body of literature [17], [18] that addresses the challenge. Note that, a small-signal converter model that takes into account the negative-sequence can be useful for stability evaluations and steady-state harmonic calculations when considering different imbalance levels. Negative-sequence voltages are known to appear during transient situations (for example, during faults); however, they may appear also during normal operation due to single-phase loads [19]–[22] and sources [23], cables in non-symmetrical arrangements (like flat formation), the lack of line transposition, and other causes. In particular, large-scale wind or solar farms are usually connected at remote locations through relatively long un-transposed lines [24] (e.g. [25]).

Further, small-signal models are sometimes used in control design. By including the effect of the negative-sequence voltage in the analysis, the model presented here, then, could become useful for the control-parameters design in the analysed control structure, which is intended to have a good performance under all levels of voltage imbalance. As shown in this paper, the overall control dynamics and especially the Phase-Locked Loop (PLL) dynamics are very much dependent on the voltage imbalance level.

Finally, this paper also addresses the impact of the negative-sequence current. In the past, several works addressed the effect of the positive-sequence current reference [6] and concluded that it has a direct impact on the stability of the converter; however, the impact of the negative-sequence current has not been analysed in the literature before. In this paper, the current imbalance level is also addressed and it is found to significantly impact the converter frequency couplings. Note that, in the presence of voltage imbalance, it is a common strategy to inject a specific set of unbalanced currents in order to eliminate the 100 Hz ripple in the instantaneous power, achieving a smoother DC voltage [26]. In parallel, a growing tendency is to design the control objectives from the grid point of view, instead of the converter point of view (i.e. in order to provide effective grid support). For this purpose, it has been shown that both sequence currents should be injected during voltage imbalance and, in fact, the injection of dual currents during unbalanced faults is a requirement that is slowly appearing explicitly in grid codes [27]. In short, it is reasonable to assume that current imbalance will accompany voltage imbalance.

In [10], harmonic linearization is used to assess the impact of voltage imbalance on the converter model; where the imbalance is characterized as a source of coupling between the positive and negative-sequence impedance of the converter. Later, it was found that the coupling essentially appears

The authors are with the DC Systems, Energy conversion and Storage Research Group (DCE&S) at the Delft University of Technology, Delft, The Netherlands (e-mails: L.BeloquiLarumbe@tudelft.nl; Z.Qin-2@tudelft.nl; L.Wang-11@tudelft.nl; P.Bauer@tudelft.nl). The corresponding author is Zian Qin (Z.Qin-2@tudelft.nl).

This work was partially funded by TKI Wind op Zee under the project Large Offshore Wind Harmonics Mitigation (LOW-HarM) by the Rijksdienst voor Ondernemend, The Netherlands.

This article has been accepted for publication in a future issue of this journal, but has not been fully edited. Content may change prior to final publication. Citation information: DOI 10.1109/TPEL.2021.3107045, IEEE Transactions on Power Electronics

between two frequencies (e.g. f_p and $2f_1 - f_\mathrm{p}$) [28]. The coupling has been shown to happen due to several reasons, such as control asymmetries in the dq channels [29]. Harmonic Transfer Function (HTF) is another approach to model the converter when confronted with imbalance [18]; however, while [18] considers the couplings created due to the asymmetrical grid, the couplings that appear within the PLL due to the Linear Time Periodic (LTP) dynamics created by the negative sequence are ignored.

Additionally, the current controller also influences the model of the converter. In order to achieve Low Voltage Ride Through (LVRT) capabilities, several approaches were developed in the past, and are reviewed in [30]. This paper is focused in one strategy called double Synchronous Reference Frame (SRF) current controller or dual current control [31], which is based on creating two dq frames, one rotating with the positive-sequence voltage and the other rotating with the negative-sequence voltage. This controller is a common choice by the industry, it is well known and has been extensively implemented [32]–[35].

The main attractiveness of the controller is that there is a direct relationship between the active and reactive power with the dq components, for which it is necessary to track the phase-angle of both the positive- and negative sequence voltages [30], [36]. There are several PLL options that can track the positive-sequence voltage [37]. However, merely a few can quickly and accurately track the negative sequence, among which the Decoupled Double SRF-PLL (DDSRF-PLL) [38] is applied in this work.

Some small-signal models of this type of current controller are already available in the literature; however, either the effect of the PLL dynamics is ignored [39] or a simple SRF-PLL design is assumed [40], [41]. Further, the effect of imbalance is overlooked.

In this paper, a small-signal model is built up for three-phase inverters with double synchronous reference frame current controller. The effect of the PLL dynamics, the grid voltage and current imbalance are all taken into account. This paper is organized as follows: Section II describes the converter under study, Section III models the converter in the frequency domain ignoring the PLL dynamics, Section IV analyses the DDSRF-PLL, and Section V presents the model of the converter considering the PLL dynamics. The analysis of the effects of imbalance on the converter frequency couplings is shown in Section VI and the model is validated in Section VII with simulations and experiments. Finally, conclusions are summarized in Section VIII.

II. Inverter Description

The PEC is shown in Fig. 1. It consists of a two-level voltage-source inverter controlled by a current loop and a PLL. The PLL follows the phase-angle of the positive-sequence voltage ($\theta_{1+} = \omega_1 t + \phi_\mathrm{vp}$) and of the negative-sequence voltage

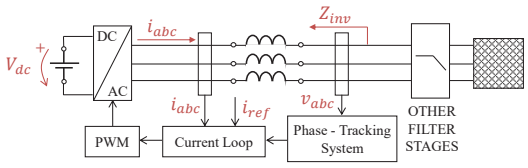

Fig. 1: Schematic of the inverter under study.

($\theta_{1-} = -\omega_1 t - \phi_\mathrm{vn}$)[1], defined in (1). The outputs of the PLL are $\theta_{\mathrm{PLL}+}$ and $\theta_{\mathrm{PLL}-}$, which in a dynamic situation might not be exactly equal to θ_{1+} and θ_{1-}. In this paper it is considered: $\theta_{\mathrm{PLL}+} = \theta_{1+} + \Delta\theta_{1+}$ and $\theta_{\mathrm{PLL}-} = \theta_{1-} + \Delta\theta_{1-}$ [7].

$$
\begin{aligned}
v_\mathrm{a}(t) &= V_\mathrm{p}\cos(\omega_1 t + \phi_\mathrm{vp}) + V_\mathrm{n}\cos(\omega_1 t + \phi_\mathrm{vn}) \\
v_\mathrm{b}(t) &= V_\mathrm{p}\cos(\omega_1 t + \phi_\mathrm{vp} - \frac{2\pi}{3}) + V_\mathrm{n}\cos(\omega_1 t + \phi_\mathrm{vn} + \frac{2\pi}{3}) \\
v_\mathrm{c}(t) &= V_\mathrm{p}\cos(\omega_1 t + \phi_\mathrm{vp} - \frac{4\pi}{3}) + V_\mathrm{n}\cos(\omega_1 t + \phi_\mathrm{vn} + \frac{4\pi}{3})
\end{aligned} \tag{1}
$$

The converter filter is an inductor L with a resistance R_L. The objective is to calculate the impedance of the inverter Z_inv (see Fig. 1). Other filter stages can be added a posteriori to Z_inv with linear circuit theory. The reference, i_ref, comes either from a user-defined command or from an outer control loop.

The current controller is shown in Fig. 2. The positive and negative-sequence currents, after a low-pass filter (LPF), G_i, and sequence decoupling, are fed to two typical PI controllers ($H_\mathrm{i} = K_\mathrm{p} + \frac{K_\mathrm{i}}{s}$) in their corresponding dq frames, respectively. A dq decoupling constant K_d (which is usually selected as $L\omega_1$) is implemented too. A voltage feed-forward loop is assumed, where an anti-aliasing filter G_v and a LPF, H_ff, are used. To prevent the risk of infinite system gain caused by the voltage feed-forward loop [35], the cut-off frequency of the H_ff is limited to $0.5\,\mathrm{Hz}$, as recommended in [42].

The control and modulation delays are modelled as $G_\mathrm{d}(s) = e^{-s1.5/f_\mathrm{s}}$, where f_s is the sampling frequency. The negative-sequence current can be filtered from the positive-sequence and vice versa through different methods. In here, a Sequence Component Decoupling Network (SCDN) similar to such in [30] is implemented. This network is shown in Fig. 3, where $F(s)$ is a LPF with a cut-off frequency ω_f (i.e., $F(s) = \frac{\omega_\mathrm{f}}{s+\omega_\mathrm{f}}$).

Literature shows that there are other options in order to achieve positive- and negative-sequence current decoupling, for example by using schemes in the $\alpha\beta$ frame [43]. On the one hand, the SCDN shown in Fig. 3 uses different dq transformations that make the SCDN dependent on the phase-tracking dynamics. In comparison, the $\alpha\beta$-frame schemes do not use this type of transformations. However, on the other hand, the $\alpha\beta$-frame schemes usually use SOGI-based algorithms, which require frequency adaptation. Therefore, the comparison in between these two approaches is not straightforward, and it

[1]Note that, in a three-phase system, it is mathematically equivalent to analyse a three-phase signal in the positive sequence with a negative frequency ($f < 0$) to analysing a three-phase signal with positive frequency ($f > 0$) in the negative sequence. Also, if the voltage is transformed into the $\alpha\beta$-frame, the negative-sequence $\alpha\beta$ vector rotates at $-\omega_1 t - \phi_\mathrm{vn}$.

This article has been accepted for publication in a future issue of this journal, but has not been fully edited. Content may change prior to final publication. Citation information: DOI 10.1109/TPEL.2021.3107045, IEEE Transactions on Power Electronics

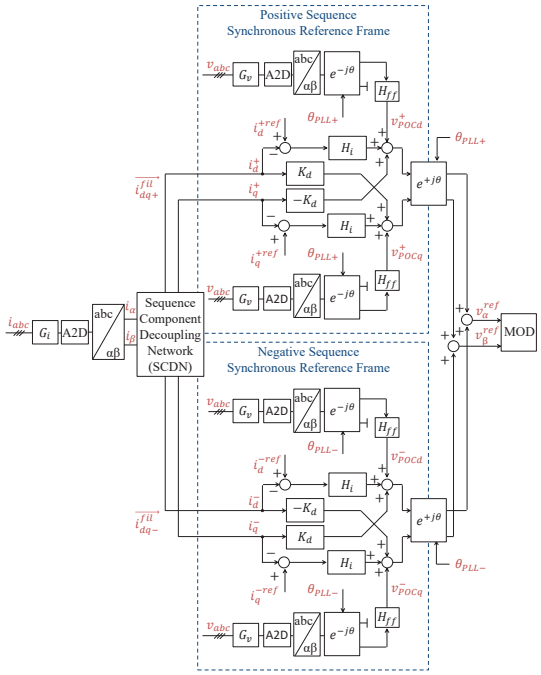

Fig. 2: Double Synchronous Reference Frame controller.

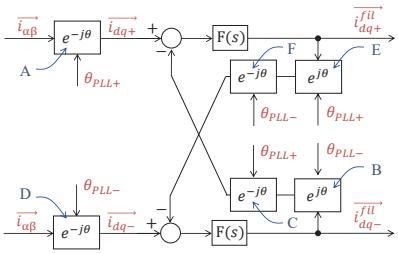

Fig. 3: Sequence Component Decoupling Network (SCDN).

is left out of the scope of this paper. In fact, the comparison of dq-based or $\alpha\beta$-based approaches for sequence decoupling could also be a subject for debate when implementing the synchronization algorithm.

In this paper, since the current loop was selected as a double synchronous reference frame control, which requires using the positive- and negative-sequence phase-angles, it was decided to choose a synchronizing structure that follows the phase-angle instead of the frequency (i.e. a PLL instead of a Frequency-Locked Loop or FLL). Literature has shown that the DDSRF-PLL and the SOGI-based PLL present similar performance during imbalance conditions [44]. The former was selected since the approach is more consistent with the current control selected. The decoupling network for the current was chosen analogously, and also due to the fact that this combination of decoupling network with this current control structure has already been proven to present good dynamic performance [30].

III. Small-Signal Model Ignoring PLL Dynamics

A. SCDN when ignoring PLL dynamics

As a first approximation, it is assumed that the PLL has perfect tracking (i.e. $\theta_{\text{PLL+}} = \theta_{1+}$ and $\theta_{\text{PLL-}} = \theta_{1-}$). Then, from Fig. 3[2]:

$$\begin{aligned}\overrightarrow{i^{\text{fil}}_{\text{dq+}}} &= (\overrightarrow{i_{\text{dq+}}} - \overrightarrow{i^{\text{fil}}_{\text{dq-}}} e^{-j(\theta_{1+}-\theta_{1-})})F(s)\\ \overrightarrow{i^{\text{fil}}_{\text{dq-}}} &= (\overrightarrow{i_{\text{dq-}}} - \overrightarrow{i^{\text{fil}}_{\text{dq+}}} e^{j(\theta_{1+}-\theta_{1-})})F(s).\end{aligned} \tag{2}$$

Operating it is possible to obtain:

$$\overrightarrow{i^{\text{fil}}_{\text{dq+}}} = F(s)\underbrace{\frac{1-F(s+j2\omega_1)}{1-F(s)F(s+j2\omega_1)}}_{\overrightarrow{G_{\text{dq+}}(s)}}\overrightarrow{i_{\text{dq+}}}. \tag{3}$$

The function $\overrightarrow{G_{\text{dec+}}(s)} = F(s)\overrightarrow{G_{\text{dq+}}(s)}$ relates the input current expressed in the positive dq frame, which has positive- and negative-sequence components, with the $\overrightarrow{i^{\text{fil}}_{\text{dq+}}}$ (the positive-sequence current expressed in the positive dq frame which does not contain the negative-sequence component). $\overrightarrow{G_{\text{dq+}}(s)}$ only depends on one parameter, ω_{f}, which is usually set as $\omega_{\text{f}} = K\omega_1 = \omega_1/\sqrt{2}$ or lower, to prevent oscillations [38].

$\overrightarrow{G_{\text{dq+}}(s)}$ has a real and an imaginary part as $\overrightarrow{G_{\text{dq+}}(s)} = G_{\text{re}}(s) + jG_{\text{im}}(s)$ defined as:

$$G_{\text{re}}(s) = \frac{(s+\omega_{\text{f}})(s^3 + 2\omega_{\text{f}}s^2 + 4{\omega_1}^2 s + 4\omega_{\text{f}}{\omega_1}^2)}{s^4 + 4\omega_{\text{f}}s^3 + 4({\omega_1}^2 + {\omega_{\text{f}}}^2)s^2 + 8{\omega_1}^2\omega_{\text{f}}s + 4{\omega_1}^2{\omega_{\text{f}}}^2} \tag{4}$$

$$G_{\text{im}}(s) = \frac{2\omega_1\omega_{\text{f}}s^2 + 2\omega_1{\omega_{\text{f}}}^2 s}{s^4 + 4\omega_{\text{f}}s^3 + 4({\omega_1}^2 + {\omega_{\text{f}}}^2)s^2 + 8{\omega_1}^2\omega_{\text{f}}s + 4{\omega_1}^2{\omega_{\text{f}}}^2}. \tag{5}$$

Similarly, $\overrightarrow{i^{\text{fil}}_{\text{dq-}}} = \overrightarrow{G_{\text{dec-}}(s)}\overrightarrow{i_{\text{dq-}}} = F(s)\overrightarrow{G_{\text{dq-}}(s)}\overrightarrow{i_{\text{dq-}}}$, where $\overrightarrow{G_{\text{dq-}}(s)} = \overrightarrow{G^*_{\text{dq+}}(s)} = G_{\text{re}}(s) - jG_{\text{im}}(s)$.

B. Inverter small-signal model when ignoring PLL dynamics

If the PLL dynamics are neglected, the inverter can be represented by the diagram in Fig. 4, where $Y_L(s) = 1/(Ls+R_L)$. In this case, taking all the complex transfer functions in the rotating frames into the $\alpha\beta$-frame is an easy procedure, since only a frequency shift has to be applied [29]. For example, the PI controller in the positive-sequence dq frame becomes $H_{\text{i}}(s - j\omega_1)$ in the $\alpha\beta$-frame, and the PI in the negative-sequence dq frame becomes $H_{\text{i}}(s + j\omega_1)$ in the $\alpha\beta$-frame.

The response of the system can be analysed from Fig. 4 by finding the transfer function from each input to the output considering that the other inputs are zero. In this case, there are 3 inputs: the two current references (one for the positive SRF and one for the negative SRF) and the voltage. In the

[2]In this paper, complex vectors and complex transfer functions are noted with an overhead arrow, as for example: $\overrightarrow{v_{\text{dq}}} = v_{\text{d}} + jv_{\text{q}}$; $\overrightarrow{v_{\alpha\beta}} = v_\alpha + jv_\beta$; $\overrightarrow{H_{\text{dq}}(s)} = H_{\text{d}}(s) + jH_{\text{q}}(s)$; and $\overrightarrow{H_{\alpha\beta}(s)} = H_\alpha(s) + jH_\beta(s)$. The upper index * denotes complex conjugate as in: $\overrightarrow{v^*_{\text{dq}}} = v_{\text{d}} - jv_{\text{q}}$ and $\overrightarrow{H^*_{\text{dq}}(s)} = H_{\text{d}}(s) - jH_{\text{q}}(s)$. The upper index $^{\text{ref}}$ is used for references.

This article has been accepted for publication in a future issue of this journal, but has not been fully edited. Content may change prior to final publication. Citation information: DOI 10.1109/TPEL.2021.3107045, IEEE Transactions on Power Electronics

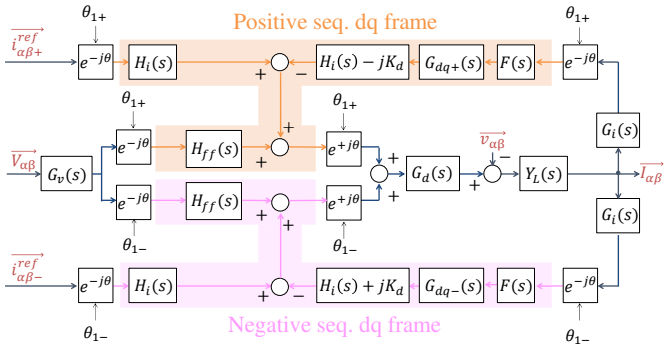

Fig. 4: Inverter schematic ignoring the PLL dynamics.

analysis below the contribution of the voltage due to the feedforward signal (related to $\overrightarrow{TF_3}$) has been separated from the contribution of the voltage due to the inner characteristics of the plant (related to $\overrightarrow{TF_4}$), leading to:

$$I_\alpha + jI_\beta = \overrightarrow{TF_1}\left(I_\alpha^{+\text{ref}} + jI_\beta^{+\text{ref}}\right) + \overrightarrow{TF_2}\left(I_\alpha^{-\text{ref}} + jI_\beta^{-\text{ref}}\right) + \overrightarrow{TF_3}\left(V_\alpha + jV_\beta\right) + \overrightarrow{TF_4}\left(V_\alpha + jV_\beta\right) \tag{6}$$

It can be seen that $\overrightarrow{TF_1}$ and $\overrightarrow{TF_2}$ are the closed-loop transfer functions of the positive and the negative sequence current; while $-\overrightarrow{TF_4}$ is the output admittance ($\overrightarrow{Y_\text{p}}$). Finally, $-\overrightarrow{TF_3}$ is the additional admittance in parallel to $-\overrightarrow{TF_4}$ that is created due voltage feedforward compensation ($\overrightarrow{Y_\text{ff}}$). Their expressions are shown (7)-(10). The impedance of the converter is shown in (11) and (12). Some of the overhead arrows in (7) – (11) are omitted for simplicity.

$$\overrightarrow{Z_{\alpha\beta-\text{frame noPLL}}} = \frac{1}{\overrightarrow{Y_\text{p}} + \overrightarrow{Y_\text{ff}}} \tag{12}$$

IV. DDSRF-PLL MODEL

The DDSRF-PLL under study is shown in Fig. 5. The ideal positive-sequence dq frame rotates at θ_{1+} and the ideal negative-sequence dq frame at θ_{1-}. The non-ideal positive-sequence and negative-sequence dq frames rotate at $\theta_{\text{PLL}+}$ and $\theta_{\text{PLL}-}$, respectively. The signals in both frames are related through (13), where the small-angle approximation is applied.

$$\begin{aligned}\overrightarrow{V_{\text{nonidealdq+}}} &= \overrightarrow{V_{\text{idealdq+}}}e^{-j\Delta\theta_{1+}} \approx \overrightarrow{V_{\text{idealdq+}}}(1 - j\Delta\theta_{1+}) \\ \overrightarrow{V_{\text{nonidealdq-}}} &= \overrightarrow{V_{\text{idealdq-}}}e^{-j\Delta\theta_{1-}} \approx \overrightarrow{V_{\text{idealdq-}}}(1 - j\Delta\theta_{1-})\end{aligned} \tag{13}$$

Each of the rotational transformations represented in Fig. 5 with the letters A, B, C, D, E, and F have to be analysed separately. For the transformation A:

$$\begin{aligned}\overrightarrow{V_{\text{nonidealdq+}}} &= \overrightarrow{V_{\text{idealdq+}}}e^{-j\Delta\theta_{1+}} \approx \overrightarrow{V_{\text{idealdq+}}}(1 - j\Delta\theta_{1+}) \\ &= \overrightarrow{V_{\text{idealdq+}}} - jV_\text{p}\Delta\theta_{1+} - jV_\text{n}e^{-j(2\omega_1 t + \phi_\text{vp} + \phi_\text{vn})}\Delta\theta_{1+}.\end{aligned} \tag{14}$$

The variable $\overrightarrow{V^{\text{fil}}_{\text{dq+}}}$ is the input to the transformation B. Since in steady-state $\overrightarrow{V^{\text{fil}}_{\text{dq-}}}$ should be approximately V_n, the output of transformation B in steady-state should be $V_\text{n}e^{-j(\omega_1 t + \phi_\text{vn})}$. Thus, the output of transformation B can be approximated as:

$$\begin{aligned}\overrightarrow{V_{\text{B}_\text{out}}} &= \overrightarrow{V^{\text{fil}}_{\text{dq-}}}e^{j\theta_{1-}}e^{j\Delta\theta_{1-}} \approx \overrightarrow{V^{\text{fil}}_{\text{dq-}}}e^{j\theta_{1-}} \\ &\quad + jV_\text{n}e^{-j(\omega_1 t + \phi_\text{vn})}\Delta\theta_{1-}.\end{aligned} \tag{15}$$

Transformation C can be found similarly:

$$\begin{aligned}\overrightarrow{V_{\text{C}_\text{out}}} &= \overrightarrow{V_{\text{B}_\text{out}}}e^{-j\theta_{1+}}e^{-j\Delta\theta_{1+}} \approx \overrightarrow{V_{\text{B}_\text{out}}}e^{-j\theta_{1+}} \\ &\quad - jV_\text{n}e^{-j(2\omega_1 t + \phi_\text{vp} + \phi_\text{vn})}\Delta\theta_{1+}.\end{aligned} \tag{16}$$

The transformations D, E and F can be found analogously, which leads to the schematic in Fig. 6. From this schematic, the following equations can be found:

$$\begin{aligned}\Delta\theta_{1+} &= \overrightarrow{V_{\text{idealdq+}}}\overrightarrow{TF_{\text{PLL1+}}} + \overrightarrow{V^*_{\text{idealdq+}}}\overrightarrow{TF_{\text{PLL2+}}} \\ &+ \overrightarrow{V_{\text{idealdq+}}}e^{j4\omega_1 t}\overrightarrow{TF_{\text{PLL3+}}} + (\overrightarrow{V_{\text{idealdq+}}}e^{j4\omega_1 t})^*\overrightarrow{TF_{\text{PLL4+}}} \\ &+ \overrightarrow{V_{\text{idealdq+}}}e^{-j4\omega_1 t}\overrightarrow{TF_{\text{PLL5+}}} + (\overrightarrow{V_{\text{idealdq+}}}e^{-j4\omega_1 t})^*\overrightarrow{TF_{\text{PLL6+}}}\end{aligned} \tag{17}$$

$$\begin{aligned}\Delta\theta_{1-} &= \overrightarrow{V_{\text{idealdq-}}}\overrightarrow{TF_{\text{PLL1-}}} + \overrightarrow{V^*_{\text{idealdq-}}}\overrightarrow{TF_{\text{PLL2-}}} \\ &+ \overrightarrow{V_{\text{idealdq-}}}e^{-j4\omega_1 t}\overrightarrow{TF_{\text{PLL3-}}} + (\overrightarrow{V_{\text{idealdq-}}}e^{-j4\omega_1 t})^*\overrightarrow{TF_{\text{PLL4-}}} \\ &+ \overrightarrow{V_{\text{idealdq-}}}e^{j4\omega_1 t}\overrightarrow{TF_{\text{PLL5-}}} + (\overrightarrow{V_{\text{idealdq-}}}e^{j4\omega_1 t})^*\overrightarrow{TF_{\text{PLL6-}}}\end{aligned} \tag{18}$$

where $\overrightarrow{TF_{\text{PLL2+}}(s)} = \overrightarrow{TF^*_{\text{PLL1+}}(s)}$, $\overrightarrow{TF_{\text{PLL4+}}(s)} = \overrightarrow{TF^*_{\text{PLL3+}}(s)}$ and $\overrightarrow{TF_{\text{PLL6+}}(s)} = \overrightarrow{TF^*_{\text{PLL5+}}(s)}$. The same applies for the complex transfer functions in (18).

In (17) and (18), it is shown that, for a perturbation in the voltage at the frequency f_p (in the positive or negative dq frame, respectively), $\Delta\theta_{1+}$ and $\Delta\theta_{1-}$ contain components at $\pm f_\text{p}$ and at $\pm f_\text{p} \pm 4f_1$. From now on, the components $\pm f_\text{p} \pm 4f_1$ are called "couplings within the PLL". These couplings are caused due to the LTP dynamics of the network. In fact, other couplings at $\pm f_\text{p} \pm 8f_1$ (and so on) were found too, but have been disregarded due to their low magnitude.

A. PLL model validation

Different simulation frequency sweeps were performed for validation purposes. In Fig. 7, it is shown how the model for $\overrightarrow{TF_{\text{PLL1+}}(s)}$ perfectly matches the frequency-sweep results for all imbalance levels. Similarly, Fig. 8 shows how the model for $\overrightarrow{TF_{\text{PLL1-}}(s)}$ is also accurate. The same applies to $\overrightarrow{TF_{\text{PLL2+}}(s)}$ and $\overrightarrow{TF_{\text{PLL2-}}(s)}$ although the figures are not shown since $\overrightarrow{TF_{\text{PLL2+}}(s)} = \overrightarrow{TF^*_{\text{PLL1+}}(s)}$ and $\overrightarrow{TF_{\text{PLL2-}}(s)} = \overrightarrow{TF^*_{\text{PLL1-}}(s)}$. Finally, the coupling transfer functions are also validated. The results are shown in Fig. 9 for the positive sequence and in Fig. 10 for the negative sequence, both for $V_\text{n} = 5\%$.

B. Couplings within the PLL

Fig. 11 shows the frequency response of the PLL transfer functions related to tracking the positive-sequence phase-angle, in the case in which $V_\text{n} = 5\%$. Only the magnitude is shown for brevity. It can be observed how $\overrightarrow{TF_{\text{PLL1+}}}$ and $\overrightarrow{TF_{\text{PLL2+}}}$ present a significantly higher magnitude than the PLL coupling transfer functions in the majority of the frequency

This article has been accepted for publication in a future issue of this journal, but has not been fully edited. Content may change prior to final publication. Citation information: DOI 10.1109/TPEL.2021.3107045, IEEE Transactions on Power Electronics

$$\overrightarrow{TF_1} = \frac{H_\mathrm{i}(s-j\omega_1)G_\mathrm{d}(s)}{Ls+R_\mathrm{L}+\left([H_\mathrm{i}(s-j\omega_1)-jK_\mathrm{d}]G_{\mathrm{dec+}}(s-j\omega_1)+[H_\mathrm{i}(s+j\omega_1)+jK_\mathrm{d}]G_{\mathrm{dec-}}(s+j\omega_1)\right)G_\mathrm{i}(s)G_\mathrm{d}(s)} \tag{7}$$

$$\overrightarrow{TF_2} = \frac{H_\mathrm{i}(s+j\omega_1)G_\mathrm{d}(s)}{Ls+R_\mathrm{L}+\left([H_\mathrm{i}(s-j\omega_1)-jK_\mathrm{d}]G_{\mathrm{dec+}}(s-j\omega_1)+[H_\mathrm{i}(s+j\omega_1)+jK_\mathrm{d}]G_{\mathrm{dec-}}(s+j\omega_1)\right)G_\mathrm{i}(s)G_\mathrm{d}(s)} \tag{8}$$

$$\overrightarrow{Y_\mathrm{p}} = -\overrightarrow{TF_4} = \frac{1}{Ls+R_\mathrm{L}+\left([H_\mathrm{i}(s-j\omega_1)-jK_\mathrm{d}]G_{\mathrm{dec+}}(s-j\omega_1)+[H_\mathrm{i}(s+j\omega_1)+jK_\mathrm{d}]G_{\mathrm{dec-}}(s+j\omega_1)\right)G_\mathrm{i}(s)G_\mathrm{d}(s)} \tag{9}$$

$$\overrightarrow{Y_\mathrm{ff}} = -\overrightarrow{TF_3} = \frac{[H_\mathrm{ff}(s-j\omega_1)+H_\mathrm{ff}(s+j\omega_1)]G_\mathrm{v}(s)G_\mathrm{d}(s)}{Ls+R_\mathrm{L}+\left([H_\mathrm{i}(s-j\omega_1)-jK_\mathrm{d}]G_{\mathrm{dec+}}(s-j\omega_1)+[H_\mathrm{i}(s+j\omega_1)+jK_\mathrm{d}]G_{\mathrm{dec-}}(s+j\omega_1)\right)G_\mathrm{i}(s)G_\mathrm{d}(s)} \tag{10}$$

$$\overrightarrow{Z_{\alpha\beta-\text{frame noPLL}}} = \frac{Ls+R_\mathrm{L}+\left([H_\mathrm{i}(s-j\omega_1)-jK_\mathrm{d}]G_{\mathrm{dec+}}(s-j\omega_1)+[H_\mathrm{i}(s+j\omega_1)+jK_\mathrm{d}]G_{\mathrm{dec-}}(s+j\omega_1)\right)G_\mathrm{i}(s)G_\mathrm{d}(s)}{1+[H_\mathrm{ff}\,(s-j\omega_1)+H_\mathrm{ff}\,(s+j\omega_1)]G_\mathrm{v}(s)G_\mathrm{d}(s)} \tag{11}$$

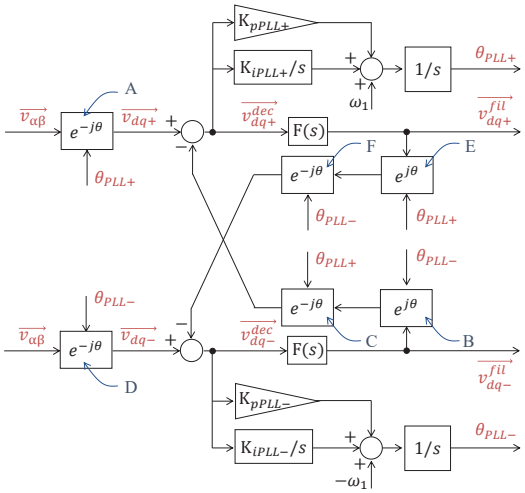

Fig. 5: DDSRF-PLL with negative sequence tracking expressed with complex transfer functions.

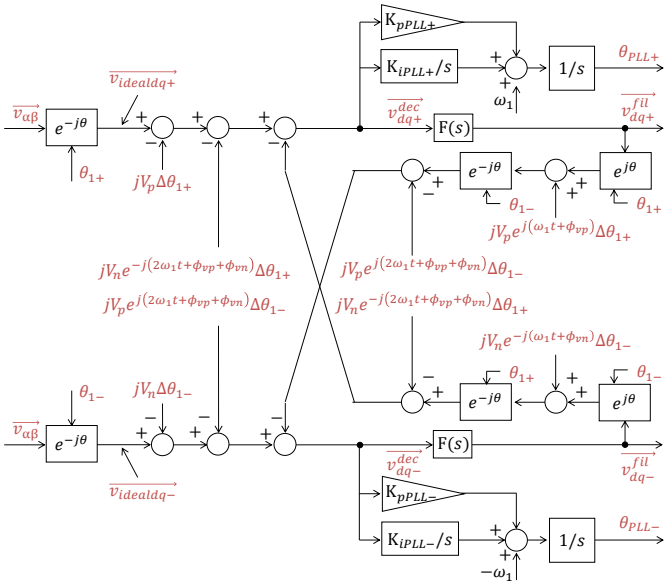

Fig. 6: PLL dynamics effect on its own decoupling network.

range. Fig. 12 shows the complex transfer functions related to tracking the negative-sequence phase-angle (also in the case in which $V_\mathrm{n} = 5\%$). In this case, the couplings are higher than in the case of tracking the positive-sequence phase-angle. Especially, $\overrightarrow{TF_{\mathrm{PLL3-}}}$ and $\overrightarrow{TF_{\mathrm{PLL4-}}}$ have a comparable magnitude to $\overrightarrow{TF_{\mathrm{PLL1-}}}$ and $\overrightarrow{TF_{\mathrm{PLL2-}}}$ in certain frequency ranges.

This is verified with a computer simulation, in which a perturbation at $f_\mathrm{p} = 200\,\mathrm{Hz}$ (frequency in the $\alpha\beta$ frame) is injected in the voltage. This component is expressed in the positive-sequence dq frame at $150\,\mathrm{Hz}$, and in the negative-sequence dq frame at $250\,\mathrm{Hz}$. On the left of Fig. 13 it is shown the positive-sequence phase-angle error created due to the perturbation in the voltage. The figure shows that $\Delta\theta_{1+}$ has only one main frequency component, at $150\,\mathrm{Hz}$. In comparison, the right part of Fig. 13 shows that $\Delta\theta_{1-}$ will have two main components: one at $250\,\mathrm{Hz}$ and a coupling at $50\,\mathrm{Hz}$. This coupling appears at approximately the same magnitude as the component at $250\,\mathrm{Hz}$, since $\overrightarrow{TF_{\mathrm{PLL3-}}}$ and $\overrightarrow{TF_{\mathrm{PLL4-}}}$ have approximately the same magnitude at $50\,\mathrm{Hz}$ and $-50\,\mathrm{Hz}$, respectively, as $\overrightarrow{TF_{\mathrm{PLL1-}}}$ and $\overrightarrow{TF_{\mathrm{PLL2-}}}$ at $250\,\mathrm{Hz}$ and $-250\,\mathrm{Hz}$, respectively (see Fig. 12). At $450\,\mathrm{Hz}$ and at $-450\,\mathrm{Hz}$, $\overrightarrow{TF_{\mathrm{PLL5-}}}$ and $\overrightarrow{TF_{\mathrm{PLL6-}}}$ have, respectively, a much lower magnitude and that is why the coupling at $450\,\mathrm{Hz}$ does not appear. The coupling generation process within the PLL for the case in which $f_\mathrm{p} = 200\,\mathrm{Hz}$ is explained in Fig. 14. As the frequency of the perturbation increases, the effect of the couplings becomes less relevant. This is shown in Fig. 15 where, for a perturbation at $f_\mathrm{p} = 400\,\mathrm{Hz}$, the couplings when tracking both phase-angles are close to zero.

C. Comparison of PLL dynamics when tracking the positive and negative phase-angle and analysis on the effect of V_n

As it is shown in Fig. 5, the DDSRF-PLL considered has a symmetrical positive- and negative-sequence design. As a consequence, the expressions for the positive and negative phase-angle dynamics (shown in (17) and (18)) are symmetrical too. However, the DDSRF-PLL is a very non-linear element that strongly depends on its operating point. Consequently, despite the expressions (17) and (18) being symmetrical, the transfer functions that appear in these expressions are not. This can be seen by comparing Fig. 7 and Fig. 8. By looking at the y-axis limits in these figures, it is clear that $\overrightarrow{TF_{\mathrm{PLL1-}}}$ is not

This article has been accepted for publication in a future issue of this journal, but has not been fully edited. Content may change prior to final publication. Citation information: DOI 10.1109/TPEL.2021.3107045, IEEE Transactions on Power Electronics

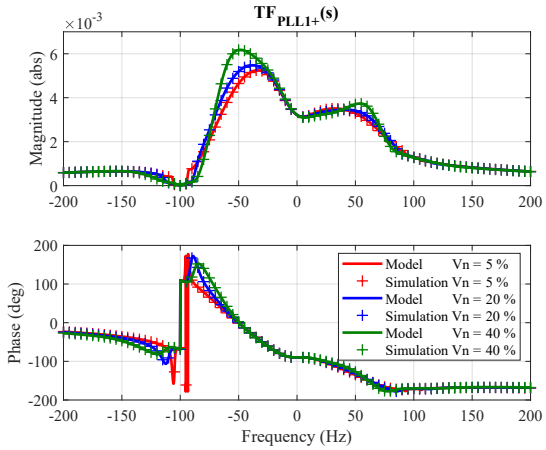

Fig. 7: Validation of PLL model for different negative-sequence voltages. $TF_{\text{PLL1+}}(s)$ shown.

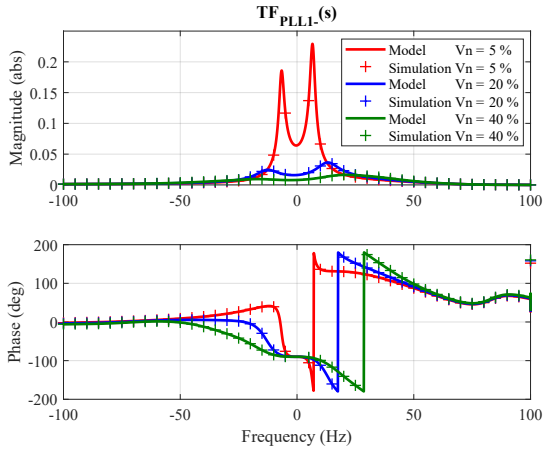

Fig. 8: Validation of PLL model for different negative-sequence voltages. $TF_{\text{PLL1-}}(s)$ shown.

the symmetrical of $\overrightarrow{TF_{\text{PLL1+}}}$. In particular, the $\overrightarrow{TF_{\text{PLL1+}}}$ and $\overrightarrow{TF_{\text{PLL2+}}}$, depend more on the positive-sequence voltage than on the negative-sequence voltage. In contrast, $\overrightarrow{TF_{\text{PLL1-}}}$ and $\overrightarrow{TF_{\text{PLL2-}}}$ are very dependent on V_{n}. Indeed, Fig. 8 shows that $\overrightarrow{TF_{\text{PLL1-}}}$ is very dependent on V_{n}, whereas Fig. 7 shows that $\overrightarrow{TF_{\text{PLL1+}}}$ is not as much.

This effect can easily understood if the whole decoupling network is ignored, and only the SRF-PLLs are addressed. A small-signal model of a SRF-PLL is shown in Fig. 16. As seen here, the small-signal model depends on the voltage V that is being followed; for the positive-sequence PLL this would be V_{p} whereas for the negative-sequence PLL it would be V_{n}.

If the couplings are analysed, a similar but opposite effect happens. The couplings that appear when tracking the positive-sequence phase-angle are due to the presence of V_{n} in the network. Therefore, $\overrightarrow{TF_{\text{PLL3+}}}$ until $\overrightarrow{TF_{\text{PLL6+}}}$ are very dependent on V_{n}. In contrast, $\overrightarrow{TF_{\text{PLL3-}}}$ until $\overrightarrow{TF_{\text{PLL6-}}}$ are very dependent on V_{p}. The coupling transfer functions when $V_{\text{n}} = 5\%$ are shown in Fig. 11 and Fig. 12, and when $V_{\text{n}} = 40\%$ are shown in Fig. 17 and Fig. 18. When V_{n} is low, the couplings in $\Delta\theta_{1-}$ are higher than in $\Delta\theta_{1+}$. When V_{n} is high, they are closer to each other.

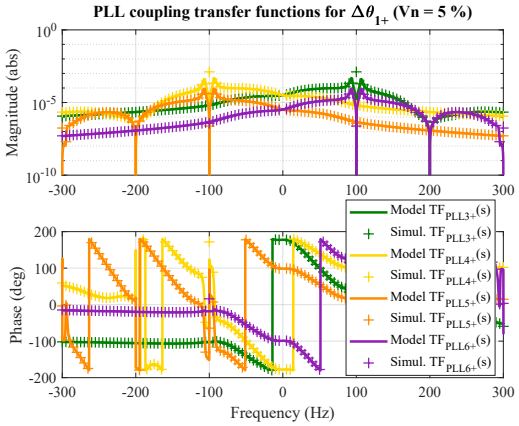

Fig. 9: Validation of PLL coupling transfer functions related to tracking the positive-sequence phase-angle ($V_{\text{n}} = 5\%$).

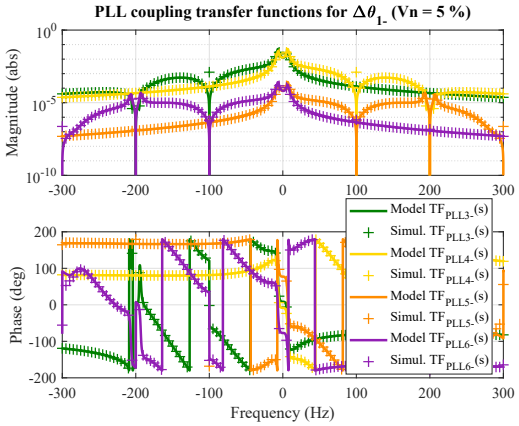

Fig. 10: Validation of PLL coupling transfer functions related to tracking the negative-sequence phase-angle ($V_{\text{n}} = 5\%$).

In general, the dynamics when tracking the positive- and negative-sequence phase-angles will only be symmetrical if $V_{\text{n}} = V_{\text{p}}$. Since this is not a realistic situation, it can be said that, despite its symmetrical design, the DDSRF-PLL presents asymmetrical dynamics.

V. Small-Signal Model Including PLL Dynamics

This section addresses the impact that the PLL dynamics have on the current control $\alpha\beta$-to-dq transformations (or vice versa). The currents in the time domain are shown in (19). As explained in the introduction, in this paper the negative-sequence currents are considered too, since it is typical to inject I_{n} in the presence of voltage imbalance.

$$\begin{aligned} i_{\text{a}}(t) &= I_{\text{p}}\cos(\omega_1 t + \phi_{\text{ip}}) + I_{\text{n}}\cos(\omega_1 t + \phi_{\text{in}}) \\ i_{\text{b}}(t) &= I_{\text{p}}\cos(\omega_1 t + \phi_{\text{ip}} - \frac{2\pi}{3}) + I_{\text{n}}\cos(\omega_1 t + \phi_{\text{in}} + \frac{2\pi}{3}) \\ i_{\text{c}}(t) &= I_{\text{p}}\cos(\omega_1 t + \phi_{\text{ip}} - \frac{4\pi}{3}) + I_{\text{n}}\cos(\omega_1 t + \phi_{\text{in}} + \frac{4\pi}{3}) \end{aligned} \quad (19)$$

This article has been accepted for publication in a future issue of this journal, but has not been fully edited. Content may change prior to final publication. Citation information: DOI 10.1109/TPEL.2021.3107045, IEEE Transactions on Power Electronics

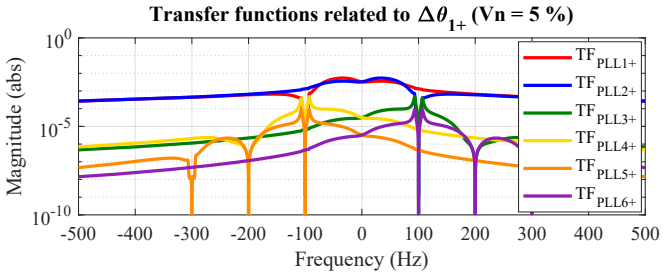

Fig. 11: Comparison of PLL transfer functions related to tracking the positive-sequence phase-angle ($V_\text{n} = 5\%$).

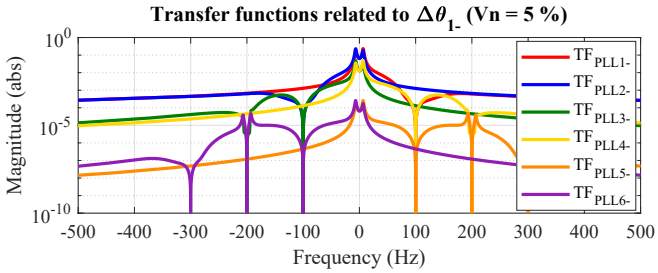

Fig. 12: Comparison of PLL transfer functions related to tracking the negative-sequence phase-angle ($V_\text{n} = 5\%$).

A. SCDN when including PLL dynamics

The effect of the DDSRF-PLL on the filtered currents $\overrightarrow{i^{\text{fil}}_{\text{dq+}}}$ and $\overrightarrow{i^{\text{fil}}_{\text{dq-}}}$ has to be addressed. In order to do that, the SCDN needs to be analysed in the same way as it was done for the DDSRF-PLL. That is to say, the transformations A, B, C, D, E and F in Fig. 3 need to be analysed separately. Following this method, this equation is obtained:

$$\begin{aligned}\overrightarrow{i^{\text{fil}}_{\text{dq+}}} = \overrightarrow{G_{\text{dec+}}(s)}\Big(&\overrightarrow{I_{\text{idealdq+}}} - jI_\text{p}e^{j(\phi_\text{ip}-\phi_\text{vp})}\Delta\theta_{1+} \\ &-jI_\text{n}e^{-j(\phi_\text{in}+\phi_\text{vp})}e^{-2j\omega_1 t}\Delta\theta_{1-}\Big).\end{aligned} \tag{20}$$

$\overrightarrow{i^{\text{fil}}_{\text{dq+}}}$ is the signal injected in the current loop (see Fig. 2). A similar expression can be found for $\overrightarrow{i^{\text{fil}}_{\text{dq-}}}$. Note in (20) that the $\overrightarrow{i^{\text{fil}}_{\text{dq+}}}$ depends on both $\Delta\theta_{1+}$ and $\Delta\theta_{1-}$.

B. Inverter small-signal model when including PLL dynamics

The rest of the frame transformations can be modelled using (21) (and the negative-sequence version of (21)) which leads to the inverter small-signal model shown in Fig. 19.

$$\begin{aligned}e^{-j\theta_{\text{PLL+}}} &= e^{-j\theta_{1+}}e^{-j\Delta\theta_{1+}} \approx e^{-j\theta_{1+}}(1-j\Delta\theta_{1+}) \\ e^{j\theta_{\text{PLL+}}} &= e^{j\theta_{1+}}e^{j\Delta\theta_{1+}} \approx e^{j\theta_{1+}}(1+j\Delta\theta_{1+})\end{aligned} \tag{21}$$

Now, the expressions for $\Delta\theta_{1+}$ and $\Delta\theta_{1-}$ shown in (17) and in (18), respectively, can be plugged in Fig. 19 to obtain the complete model. By doing this, it can be seen that the PLL dynamics, through $\Delta\theta_{1+}$ and $\Delta\theta_{1-}$, introduce in the current

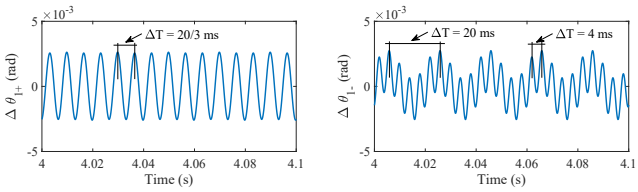

Fig. 13: Positive- and negative-sequence phase-angle error created due to a perturbation in the voltage at $f_\text{p} = 200\,\text{Hz}$ ($V_\text{n} = 5\%$).

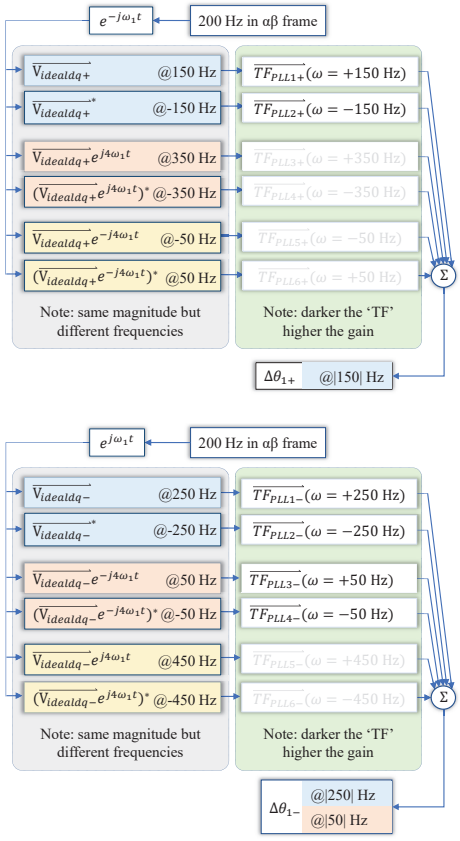

Fig. 14: Explanation of the couplings within the PLL due to a perturbation in the voltage at $f_\text{p} = 200\,\text{Hz}$ ($V_\text{n} = 5\%$).

control the voltage vector $\overrightarrow{V_{\alpha\beta}}$ conjugated, frequency shifted or both. This means that, for a single frequency component in $\overrightarrow{V_{\alpha\beta}}$, multiple frequency components will appear in the current, phenomenon that is usually called frequency coupling. Some of these frequency couplings, however, may be ignored due to their low magnitude. The detailed reasoning for this is provided in Section VI-C. In the end, two main frequency couplings appear in the converter: one through $\overrightarrow{V^*_{\alpha\beta}}e^{j2\omega_1 t}$ and one through $\overrightarrow{V^*_{\alpha\beta}}e^{-j2\omega_1 t}$.

Therefore, from Fig. 19, the following equation is obtained:

$$\begin{aligned}\overrightarrow{I_{\alpha\beta}} = \overrightarrow{TF_1}\overrightarrow{I^{+\text{ref}}_{\alpha\beta}} + \overrightarrow{TF_2}\overrightarrow{I^{-\text{ref}}_{\alpha\beta}} \\ +\overrightarrow{TF_3}\overrightarrow{V_{\alpha\beta}} + \overrightarrow{TF_4}\overrightarrow{V_{\alpha\beta}} + \overrightarrow{TF_5}\overrightarrow{V_{\alpha\beta}} + \overrightarrow{TF_6}\overrightarrow{V_{\alpha\beta}} \\ +\overrightarrow{TF_7}\overrightarrow{V^*_{\alpha\beta}}e^{j2\omega_1 t} + \overrightarrow{TF_8}\overrightarrow{V^*_{\alpha\beta}}e^{-j2\omega_1 t}.\end{aligned} \tag{22}$$

This article has been accepted for publication in a future issue of this journal, but has not been fully edited. Content may change prior to final publication. Citation information: DOI 10.1109/TPEL.2021.3107045, IEEE Transactions on Power Electronics

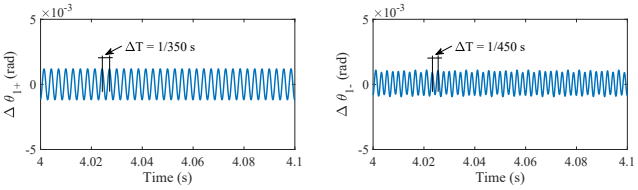

Fig. 15: Positive- and negative-sequence phase-angle error created due to a perturbation in the voltage at $f_\mathrm{p} = 400\,\mathrm{Hz}$ ($V_\mathrm{n} = 5\%$).

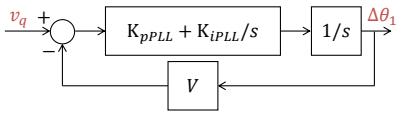

Fig. 16: Small-signal model of a generic SRF-PLL when tracking a positive- or a negative-sequence phase-angle.

In Fig. 19, it is shown how extra inputs of $\overrightarrow{V_{\alpha\beta}}$ appear due to $\Delta\theta_{1+}$. These contributions are grouped in $\overrightarrow{TF_5}$. Similarly, the extra inputs of $\overrightarrow{V_{\alpha\beta}}$ that appear due to $\Delta\theta_{1-}$ are grouped in $\overrightarrow{TF_6}$. The effect of $\overrightarrow{TF_5}$ and $\overrightarrow{TF_6}$ is to add admittances in parallel to the total admittance of the converter (see (23)). Thus, the final impedance of the converter taking into account the phase-tracking system dynamics can be calculated with (24). The expressions for $\overrightarrow{TF_5}$ and $\overrightarrow{TF_6}$ are not shown for brevity, but the final expression for the converter impedance is shown in (25), where the terms $\overrightarrow{A(s)}$ and $\overrightarrow{B(s)}$ are defined in (28) and (29).

$$\overrightarrow{Y_{\mathrm{PLL+}}(s)} = -\overrightarrow{TF_5}\,;\; \overrightarrow{Y_{\mathrm{PLL-}}(s)} = -\overrightarrow{TF_6} \tag{23}$$

$$\overrightarrow{Z_{\alpha\beta-\mathrm{frame}}} = \frac{1}{\overrightarrow{Y(s)}} = \frac{1}{\overrightarrow{Y_\mathrm{p}} + \overrightarrow{Y_\mathrm{ff}} + \overrightarrow{Y_{\mathrm{PLL+}}} + \overrightarrow{Y_{\mathrm{PLL-}}}} \tag{24}$$

$$\begin{aligned}\overrightarrow{A(s)} = {} & jI_\mathrm{p}e^{j(\phi_\mathrm{ip}-\phi_\mathrm{vp})}[H_\mathrm{i}(s-j\omega_1) - jK_\mathrm{d}]G_{\mathrm{dec+}}(s-j\omega_1) \\ & + jI_\mathrm{p}e^{j(\phi_\mathrm{ip}-\phi_\mathrm{vp})}[H_\mathrm{i}(s+j\omega_1) + jK_\mathrm{d}]G_{\mathrm{dec-}}(s+j\omega_1) \\ & - jV_\mathrm{p}H_\mathrm{ff}(s-j\omega_1)G_\mathrm{v}(s) + j(I_\mathrm{p}e^{j(\phi_\mathrm{ip}-\phi_\mathrm{vp})}(R_\mathrm{L} + jL\omega_1) + V_\mathrm{p})\end{aligned} \tag{28}$$

$$\begin{aligned}\overrightarrow{B(s)} = {} & jI_\mathrm{n}e^{-j(\phi_\mathrm{in}-\phi_\mathrm{vn})}[H_\mathrm{i}(s+j\omega_1) + jK_\mathrm{d}]G_{\mathrm{dec-}}(s+j\omega_1) \\ & + jI_\mathrm{n}e^{-j(\phi_\mathrm{in}-\phi_\mathrm{vn})}[H_\mathrm{i}(s-j\omega_1) - jK_\mathrm{d}]G_{\mathrm{dec+}}(s-j\omega_1) \\ & - jV_\mathrm{n}H_\mathrm{ff}(s+j\omega_1)G_\mathrm{v}(s) + j(I_\mathrm{n}e^{-j(\phi_\mathrm{in}-\phi_\mathrm{vn})}(R_\mathrm{L} - jL\omega_1) + V_\mathrm{n})\end{aligned} \tag{29}$$

The vectors $\overrightarrow{V^*_{\alpha\beta}}e^{j2\omega_1 t}$ and $\overrightarrow{V^*_{\alpha\beta}}e^{-j2\omega_1 t}$ are related to the output current through $\overrightarrow{TF_7}$ and $\overrightarrow{TF_8}$, that are the negated version of the coupling admittances, shown in (26) and (27). Some overhead arrows in (25) – (29) are omitted for simplicity.

In previous literature [29], it was already shown how the PLL dynamics may produce a frequency coupling through $\overrightarrow{V^*_{\alpha\beta}}e^{j2\omega_1 t}$ (i.e., for a perturbation in the voltage f_p the current has a frequency component at $f_{\mathrm{c1}} = 2f_1 - f_\mathrm{p}$). What this paper shows is that, in the cases in which the PLL also tracks the

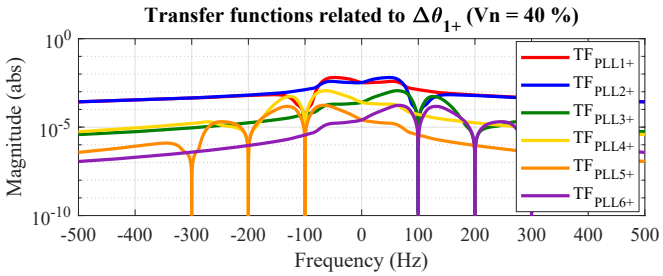

Fig. 17: Comparison of PLL transfer functions related to tracking the positive-sequence phase-angle ($V_\mathrm{n} = 40\%$).

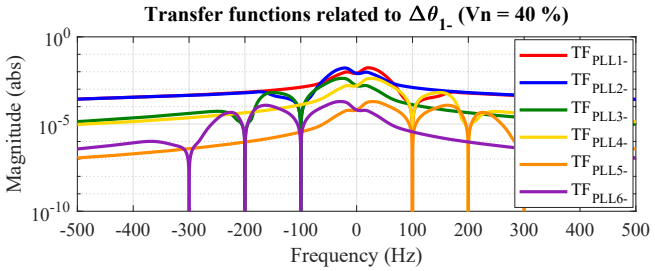

Fig. 18: Comparison of PLL transfer functions related to tracking the negative-sequence phase-angle ($V_\mathrm{n} = 40\%$).

negative-sequence phase-angle, the PLL dynamics produce an extra coupling at $f_{\mathrm{c2}} = -2f_1 - f_\mathrm{p}$, as illustrated in Fig. 20.

VI. Frequency Couplings

A. Effect of V_n and I_n on the frequency couplings

In order to understand the coupling generation process, and how it is affected by the voltage and current imbalance, different simulations were made in which a perturbation is set in the voltage and the current spectrum is acquired. The converter parameters are the same as in the laboratory prototype, and are listed in Table I. The perturbation frequency f_p was selected as $-30\,\mathrm{Hz}$ because at this point, for the parameters selected and if $V_\mathrm{n} = 5\,\%$ and $I_\mathrm{p} = I_\mathrm{n} = 5\,\mathrm{A}$, the coupling admittances are approximately equal in magnitude (i.e. $|\overrightarrow{Y_{\mathrm{c1}}(s)}|$ at $2f_1 - f_\mathrm{p} = 130\,\mathrm{Hz}$ is approximately equal to $|\overrightarrow{Y_{\mathrm{c2}}(s)}|$ at $-2f_1 - f_\mathrm{p} = -70\,\mathrm{Hz}$). The simulations were performed with a continuous model in the s-domain without switches, in order to have cleaner results and avoid possible switching and modulation couplings.

The results are shown in Fig. 21 and Fig. 22. First of all, in Fig. 21 a) it can be seen that, even in the case where the negative-sequence voltage is relatively low and the negative-sequence current is equal to zero, the second frequency coupling exists. This is due to the fact that this second frequency coupling is not directly due to the presence of V_n, but rather to the use of $\theta_{\mathrm{PLL-}}$ in the current control loop, as it will be explained in detail in Section VI-B. By comparing Fig. 21 and Fig. 22, however, it can be seen that, when the voltage imbalance is low, the second frequency coupling depends significantly on the negative-sequence current. With a

This article has been accepted for publication in a future issue of this journal, but has not been fully edited. Content may change prior to final publication. Citation information: DOI 10.1109/TPEL.2021.3107045, IEEE Transactions on Power Electronics

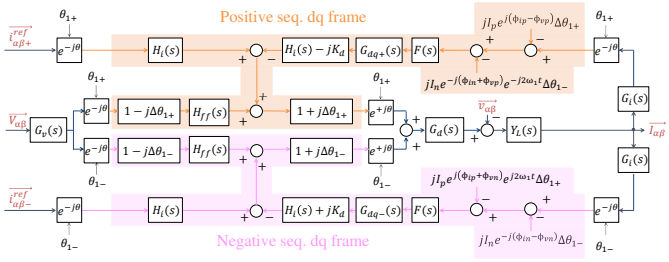

Fig. 19: Inverter schematic considering the PLL dynamics.

higher I_n, the component at $-2f_1 - f_p$ considerably increases. This is due to the fact that, for a low V_n, the $\overrightarrow{TF_{PLL2-}}$ is very high (see Fig. 8) and therefore, it has a big impact on $\overrightarrow{Y_{c2}}$. Since $\overrightarrow{B(s)}$ multiplies $\overrightarrow{TF_{PLL2-}}$, changing I_n has a big impact on $\overrightarrow{Y_{c2}}$. This strengthens the idea that considering the impact of the current imbalance is important for the dynamic modelling of converters.

In Fig. 22 it can be seen that, once the voltage imbalance is increased, the second frequency coupling considerably increases too, becoming bigger than the first frequency coupling and even bigger than the component at -30 Hz. Additionally, it is noticeable that, in the case of high voltage imbalance, other frequency couplings start to appear (in this case, for example, at 170 Hz) due to the LTP dynamics of the DDSRF-PLL. A question arises, then, as to how many couplings should be considered in the final converter model. This is addressed in detail in Section VI-C.

A similar work was performed in the laboratory set-up, and the results are shown in Fig. 23. This figure shows the contrast in the current spectrum when there is a perturbation in the voltage or not. When there is no perturbation, the results are shown in Fig. 23 a) and the current only has the fundamental component and a harmonic at 150 Hz, which is probably due to the effect of the voltage imbalance through the DC voltage. This component does not appear in the simulations since in the simulations the effect of the DC voltage is neglected. This effect has been reported in the literature before [17]. When the perturbation is injected, it is shown in Fig. 23 b) that two frequency couplings appear, as predicted in this paper. Note also that, the magnitude of the harmonics at 70 Hz and 130 Hz are shown at the bottom of the oscilloscope images, where it can be seen quantitatively that the harmonics at these frequencies increase when there is a perturbation at -30 Hz.

The results in Fig. 23 b) are the same as the simulation results in Fig. 21 b). The only difference is that the oscilloscope cannot perform the FFT of the currents in the three-phases, and thus the sequence of the harmonics cannot be calculated by the oscilloscope. That is why in Fig. 23 the sequence of the harmonics is not shown. The frequencies, however, perfectly match with the analysis in this paper.

B. Origin of the second frequency coupling

In comparison to previous literature, one key difference in this paper is that it considers a PLL structure that also tracks the negative-sequence phase-angle. In particular, it is shown here that, even if the couplings within the PLL are ignored, the θ_{PLL-} has the frequencies $\pm(f_p + f_1)$. Consequently, if θ_{PLL-} is used in the construction of the current control loop, then an additional frequency coupling at $-2f_1 - f_p$ appears (as illustrated in Fig. 20). Therefore, the frequency coupling is not directly due to the presence of V_n. However, the presence of V_n is necessary since otherwise the negative-sequence phase-angle is undefined and therefore it cannot be used to construct the negative-sequence SRF for the current control, yielding impossible for this second frequency coupling to appear. In a sense, a similar situation happens with the first frequency coupling: the PLL dynamics create the coupling at $2f_1 - f_p$, although it is true that the presence of V_p is a pre-assumed condition so that θ_{1+} is defined.

In order to show more intuitively that the second frequency coupling is due to the use of θ_{PLL-} in the current control loop, another simulation was done with a slightly different DDSRF-PLL. In this case, the DDSRF-PLL tracks only the positive-sequence phase-angle, and the negative-sequence phase-angle is simply calculated by imposing: $\theta_{PLL-} = -\theta_{PLL+}$. In these conditions, the equivalent simulation as the one shown in Fig. 21 b) was done. The results are shown in Fig. 24.

As it can be seen, the current presents no longer the second frequency coupling. This can be understood by looking at Fig. 15. If the voltage has a perturbation at $f_p = 400$ Hz, when the DDSRF-PLL in Fig. 5 is used, a 350 Hz oscillation can be seen in θ_{PLL+} and a different oscillation (at 450 Hz) can be seen in θ_{PLL-}. This is a different situation from the case in which $\theta_{PLL-} = -\theta_{PLL+}$ since, then, the oscillation at θ_{PLL-} will be seen at 350 Hz. Therefore, it is clear that the second frequency coupling is not due to the use of a negative-sequence dq frame in the current control, but rather due to the use of θ_{PLL-} in the current control.

C. Number of frequency couplings

The LTP dynamics of the PLL have been considered in this paper. It is shown here that the first round of couplings will appear at $f_p^{dq+} \pm 4f_1$ for θ_{PLL+} and at $f_p^{dq-} \pm 4f_1$ for θ_{PLL-}. Once the whole converter is considered, numerous frequency couplings are predicted in the calculations. In particular, when looking into Fig. 19 it can be seen that, in several instances, $\Delta\theta_{1+}$ or $\Delta\theta_{1-}$ appear in the small-signal model of the current control. In total, 13 couplings may appear in the output current: $f_{c1} = 2f_1 - f_p$, $f_{c2} = -2f_1 - f_p$, $f_{c3} = 2f_1 + f_p$, $f_{c4} = -2f_1 + f_p$, $f_{c5} = 4f_1 - f_p$, $f_{c6} = -4f_1 - f_p$, $f_{c7} = 4f_1 + f_p$, $f_{c8} = -4f_1 + f_p$, $f_{c9} = 6f_1 - f_p$, $f_{c10} = -6f_1 - f_p$, $f_{c11} = 6f_1 + f_p$, $f_{c12} = -6f_1 + f_p$, and $f_{c13} = -f_p$.

A question arises as to how many couplings should be considered in the model. In order to solve this, different simulations were done in which a perturbation was imposed in the voltage at different frequencies, and the coupling currents were measured. The results are shown in Fig. 25.

As it can be seen in Fig. 25 a), when $V_n = 5\%$, all the frequency couplings are very low in the whole frequency range, except for $f_{c1} = 2f_1 - f_p$ and $f_{c2} = -2f_1 - f_p$. When V_n increases, as it was shown in Section IV-C, the couplings in $\Delta\theta_{1+}$ increase. This results in $f_{c7} = 4f_1 + f_p$ and $f_{c8} =$

$$\overrightarrow{Z_{\alpha\beta-\text{frame}}} = \frac{Ls + R_\text{L} + \left([H_\text{i}(s-j\omega_1) - jK_\text{d}]G_{\text{dec+}}(s-j\omega_1) + [H_\text{i}(s+j\omega_1) + jK_\text{d}]G_{\text{dec-}}(s+j\omega_1)\right)G_\text{i}(s)G_\text{d}(s)}{1 + \Big([H_\text{ff}(s-j\omega_1) + H_\text{ff}(s+j\omega_1)]G_\text{v}(s) - A(s)TF_{\text{PLL1+}}(s-j\omega_1) - B(s)TF_{\text{PLL1-}}(s+j\omega_1)\Big)G_\text{d}(s)} \tag{25}$$

$$\overrightarrow{Y_{\text{c1}\alpha\beta-\text{frame}}(s)} = \frac{\Big(-A(s)TF_{\text{PLL2+}}(s-j\omega_1)e^{j2\phi_\text{vp}} - B(s)TF_{\text{PLL4-}}(s+j\omega_1)e^{-j2\phi_\text{vn}}\Big)G_\text{d}(s)}{Ls + R_\text{L} + \left([H_\text{i}(s-j\omega_1) - jK_\text{d}]G_{\text{dec+}}(s-j\omega_1) + [H_\text{i}(s+j\omega_1) + jK_\text{d}]G_{\text{dec-}}(s+j\omega_1)\right)G_\text{i}(s)G_\text{d}(s)} \tag{26}$$

$$\overrightarrow{Y_{\text{c2}\alpha\beta-\text{frame}}(s)} = \frac{\Big(-B(s)TF_{\text{PLL2-}}(s+j\omega_1)e^{-j2\phi_\text{vn}} - A(s)TF_{\text{PLL4+}}(s-j\omega_1)e^{j2\phi_\text{vp}}\Big)G_\text{d}(s)}{Ls + R_\text{L} + \left([H_\text{i}(s-j\omega_1) - jK_\text{d}]G_{\text{dec+}}(s-j\omega_1) + [H_\text{i}(s+j\omega_1) + jK_\text{d}]G_{\text{dec-}}(s+j\omega_1)\right)G_\text{i}(s)G_\text{d}(s)} \tag{27}$$

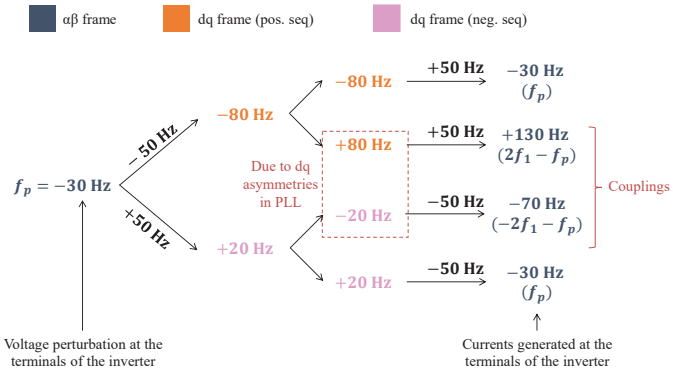

Fig. 20: Frequency coupling generation process.

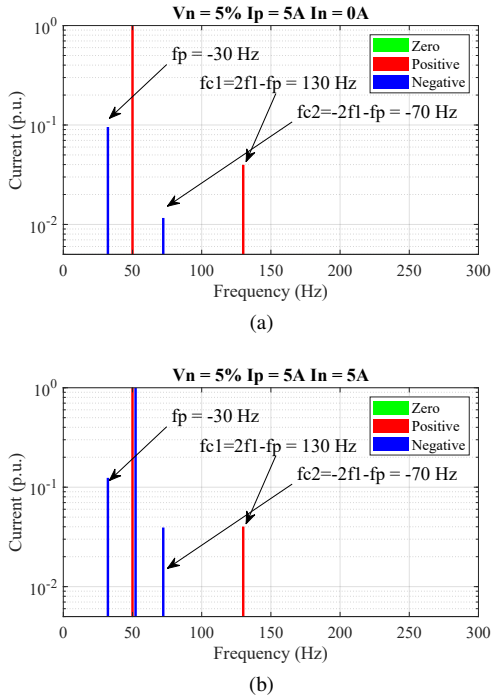

Fig. 21: Current spectrum as a result of a voltage with perturbation at $f_\text{p} = -30\,\text{Hz}$ for $V_\text{n} = 5\%$. a) $I_\text{p} = 5\,\text{A}$ $I_\text{n} = 0\,\text{A}$; b) $I_\text{p} = 5\,\text{A}$ $I_\text{n} = 5\,\text{A}$. These results are from simulation.

$-4f_1 + f_\text{p}$ increasing, so they start to be noticeable. However, it can be seen in Fig. 22 that $f_{\text{c}7} = 4f_1 + f_\text{p} = 170\,\text{Hz}$ is still considerably smaller than the other couplings (note that the y-axis is logarithmic).

Therefore, it was concluded in this paper that considering only $f_{\text{c}1} = 2f_1 - f_\text{p}$ and $f_{\text{c}2} = -2f_1 - f_\text{p}$ was sufficient to achieve enough accuracy. These couplings are mostly created by $\overrightarrow{TF_{\text{PLL2+}}}$ and $\overrightarrow{TF_{\text{PLL2-}}}$, and therefore are not due to the LTP dynamics of the DDSRF-PLL. However, since in some instances, some of the couplings within the PLL appeared at these exact frequencies ($2f_1 - f_\text{p}$ and $-2f_1 - f_\text{p}$), then they were considered in the final expression of $\overrightarrow{Y_{\text{c}1}}$ and $\overrightarrow{Y_{\text{c}2}}$ (in particular, $\overrightarrow{TF_{\text{PLL4+}}}$ and $\overrightarrow{TF_{\text{PLL4-}}}$). However, it is worth to note that the contribution of $\overrightarrow{TF_{\text{PLL4-}}}$ and $\overrightarrow{TF_{\text{PLL4+}}}$ to $\overrightarrow{Y_{\text{c}1}}$ and $\overrightarrow{Y_{\text{c}2}}$, respectively, is much smaller than such of $\overrightarrow{TF_{\text{PLL2+}}}$ and $\overrightarrow{TF_{\text{PLL2-}}}$, respectively.

In any case, if a very accurate model of the converter is desired, other frequency couplings may be included in the analysis, albeit with the drawback of handling a more complex converter model. In the end, depending on the application, a different decision might be made depending on the trade-off between accuracy versus complexity.

VII. Simulation and Experimental Validation

A. Simulation and experiment description

In order to verify the model, several computer-simulated and experimental frequency sweeps were performed. The converter parameters are the same in the computer model as in the laboratory prototype, and are listed in Table I. The laboratory set-up is shown in Fig. 26. The grid emulator generates the fundamental voltage with the appropriate imbalance level depending on the case study and also the necessary perturbation for the frequency sweep. The three-phase inverter is controlled with a current loop and a PLL as described in this paper.

B. Results

The intention is to validate the model for different PLL parameters and for different voltage and current imbalance situations. In order to do that, the following case studies are defined:

- Case A: $\text{BW}_\text{PLL} = 30\,\text{Hz}$; $V_\text{n} = 5\,\%$; $I_\text{p} = I_\text{n} = 5\,\text{A}$
- Case B: $\text{BW}_\text{PLL} = 10\,\text{Hz}$; $V_\text{n} = 5\,\%$; $I_\text{p} = I_\text{n} = 5\,\text{A}$
- Case C: $\text{BW}_\text{PLL} = 30\,\text{Hz}$; $V_\text{n} = 40\,\%$; $I_\text{p} = I_\text{n} = 5\,\text{A}$

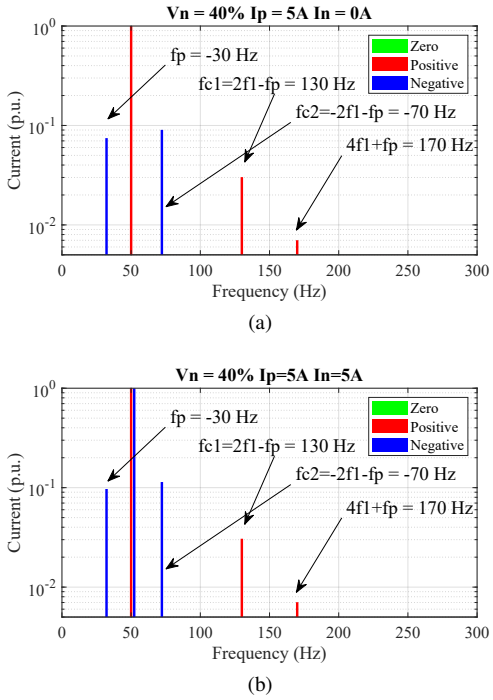

Fig. 22: Current spectrum as a result of a voltage with perturbation at $f_\mathrm{p} = -30\,\mathrm{Hz}$ for $V_\mathrm{n} = 40\%$. a) $I_\mathrm{p} = 5\,\mathrm{A}$ $I_\mathrm{n} = 0\,\mathrm{A}$; b) $I_\mathrm{p} = 5\,\mathrm{A}$ $I_\mathrm{n} = 5\,\mathrm{A}$. These results are from simulation.

TABLE I: Inverter parameters

	Description	Value	Unit
V_dc	DC Voltage	500	V
V_phase	Phase Voltage	110	V
L	Output Inductor	5	mH
R_L	Resistance of Output Inductor	44	mΩ
f_sw	Switching Frequency	20	kHz
f_s	Sampling Frequency	20	kHz
K_p	Proportional Constant PI Current	4.7	Ω
K_i	Integral Constant PI Current	41.5	Ω/s

- Case D: $\mathrm{BW_{PLL}} = 30\,\mathrm{Hz}$; $V_\mathrm{n} = 5\,\%$; $I_\mathrm{p} = I_\mathrm{n} = 10\,\mathrm{A}$
- Case E: $\mathrm{BW_{PLL}} = 30\,\mathrm{Hz}$; $V_\mathrm{n} = 5\,\%$; $I_\mathrm{p} = 5\,\mathrm{A}$; $I_\mathrm{n} = 0\,\mathrm{A}$

From now on, case A is the base case[3]. In case B, the PLL parameters are modified. In case C, the negative-sequence voltage is increased. In cases A – C the current references are kept constant as $I_\mathrm{d+ref} = I_\mathrm{d-ref} = 5\,\mathrm{A}$ and $I_\mathrm{q+ref} = I_\mathrm{q-ref} = 0\,\mathrm{A}$ in order to achieve $I_\mathrm{p} = I_\mathrm{n} = 5\,\mathrm{A}$. In cases D and E these current references are modified.

The results of these frequency sweeps are shown in Fig. 27 – Fig. 31 for the different case studies. Firstly, Fig. 27 shows that the analytical model (line) perfectly matches the simulation

[3]In case A the PLL constants are: $K = 1/\sqrt{2}$, $K_\mathrm{pPLL+} = K_\mathrm{pPLL-} = 1.71$, $K_\mathrm{iPLL+} = K_\mathrm{iPLL-} = 228.4$. In case B the PLL constants are: $K = 1/2$, $K_\mathrm{pPLL+} = K_\mathrm{pPLL-} = 0.57$, $K_\mathrm{iPLL+} = K_\mathrm{iPLL-} = 25.4$. The figures in Sections IV and VI were obtained with the PLL parameters of case A.

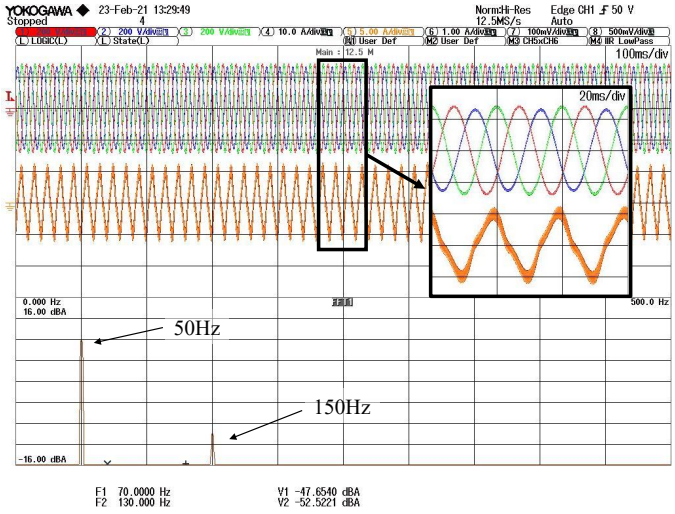

Fig. 23: Current spectrum when $I_\mathrm{p} = 5\,\mathrm{A}$ $I_\mathrm{n} = 5\,\mathrm{A}$ ($V_\mathrm{n} = 5\%$). a) No perturbation; b) Perturbation in the voltage at $f_\mathrm{p} = -30\,\mathrm{Hz}$. The x-axis expands from $0\,\mathrm{Hz}$ until $500\,\mathrm{Hz}$ in increments of $50\,\mathrm{Hz}$. These results are from experiments.

results (crosses) for the impedance and both admittances[4]. The experimental results (circles) also match the analytical model and the simulations for the impedance and for both coupling admittances, although, for the coupling admittances, the phase-angle plot of the experiment results shows some deviation. This is mostly due to the limitations of the current probe for low currents (the perturbation in the voltage was set around $0.5 - 1\,\mathrm{V}$, and thus the currents to be measured for the coupling admittances were on the range of a few dozens of mA or lower). The difficulty in this measurement lies not only in the low magnitude of the currents to be measured, but also in the fact that they have to be measured in a signal that is dominated by the fundamental, which is several orders

[4]In reality, Fig. 27 – Fig. 31 show the inverse of the impedance, $\overrightarrow{Y(s)} = 1/\overrightarrow{Z_{\alpha\beta-\mathrm{frame}}}$ for easier comparison with the coupling admittances. Note that, if the admittance is accurate, the impedance should be accurate too.

This article has been accepted for publication in a future issue of this journal, but has not been fully edited. Content may change prior to final publication. Citation information: DOI 10.1109/TPEL.2021.3107045, IEEE Transactions on Power Electronics

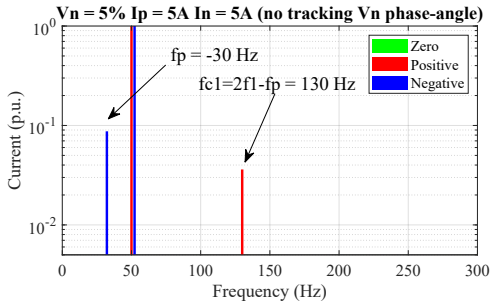

Fig. 24: Current spectrum as a result of a voltage with perturbation at $f_\mathrm{p} = -30\,\mathrm{Hz}$ for $V_\mathrm{n} = 5\%$, $I_\mathrm{p} = 5\,\mathrm{A}$ $I_\mathrm{n} = 5\,\mathrm{A}$. These results are from simulation. The negative-sequence phase-angle is not tracked.

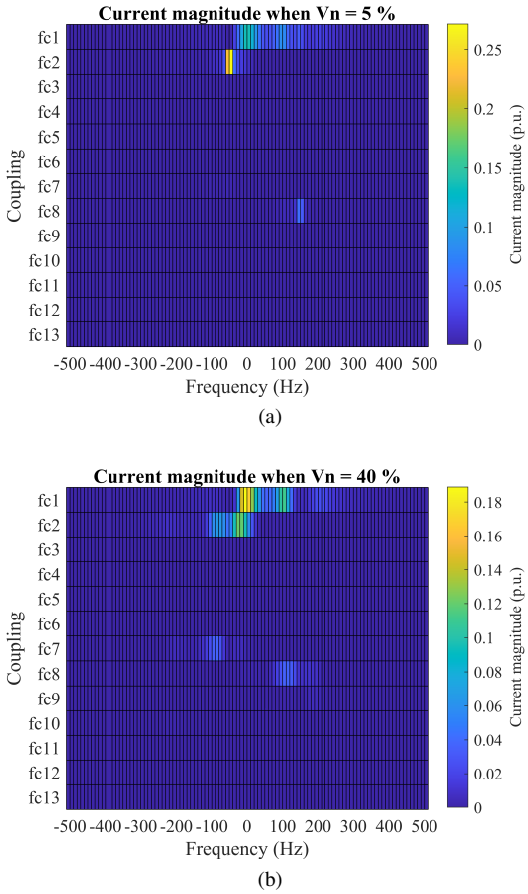

Fig. 25: Magnitude of the current coupling at different frequencies when $I_\mathrm{p} = 5\,\mathrm{A}$ $I_\mathrm{n} = 5\,\mathrm{A}$. a) $V_\mathrm{n} = 5\%$; b) $V_\mathrm{n} = 40\%$. These results are from simulations.

of magnitude higher (several A). In fact, note that, when the admittance magnitude is higher, and thus the currents to be measured are higher, the phase-angles obtained in the experiments match perfectly the analytical and simulation results. The experimental results only show some deviations when the admittance value is around or below $-30\,\mathrm{dB}$ approximately. Similar conclusions can be reached in all the other case studies, which means that the model presented in this paper is accurate for different PLL bandwidths (case B), different

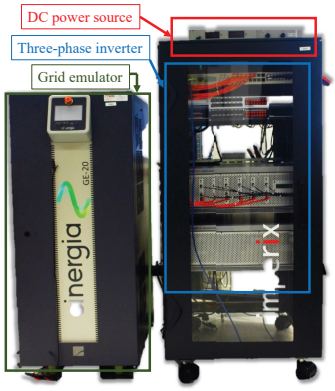

Fig. 26: Laboratory set-up.

levels of voltage imbalance (case C), different output currents (case D) and different levels of current imbalance (case E).

The results in Section VI-A show how the current and voltage imbalance considerably impact the converter couplings. By comparing Fig. 27 – Fig. 31, this section also shows how the main impedance (and coupling admittances) of the converter are modified depending on the imbalance and PLL parameters.

VIII. Conclusions

A small-signal model for power-electronics converters that use a double Synchronous Reference Frame current control is developed and validated in this paper, with simulation and experimental results. The model is shown to be valid for different levels of voltage and current imbalance. The impact of the negative-sequence voltage and current on the converter frequency couplings is analysed. It is found that the voltage-imbalance level can have a considerable impact in the PLL dynamics, which should be taken into account for the PLL constants design. It is further revealed that the negative-sequence voltage and current have a relevant effect on the main impedance or admittance of the converter, and also on the coupling admittances. In short, the voltage and current imbalance levels modify the operating point of the converter and, therefore, its linearized dynamics change. Due to the use of the negative-sequence voltage phase-angle in the current control, an additional frequency coupling at $-2f_1 - f_\mathrm{p}$ appears.

References

[1] B. Ferreira, "Understanding the Challenges of Converter Networks and Systems: Better opportunities in the future," *IEEE Power Electronics Magazine*, vol. 3, no. 2, pp. 46–49, Jun. 2016.

[2] J. H. R. Enslin and P. J. M. Heskes, "Harmonic interaction between a large number of distributed power inverters and the distribution network," *IEEE Transactions on Power Electronics*, vol. 19, no. 6, pp. 1586–1593, Nov. 2004.

[3] J. L. Agorreta, M. Borrega, J. López, and L. Marroyo, "Modeling and control of N-paralleled grid-connected inverters with LCL filter coupled due to grid impedance in PV plants," *IEEE Transactions on Power Electronics*, vol. 26, no. 3, pp. 770–785, Mar. 2011.

[4] C. Buchhagen, C. Rauscher, A. Menze, and J. Jung, "Borwin1 — first experiences with harmonic interactions in converter dominated grids," in *International ETG Congress 2015; Die Energiewende - Blueprints for the new energy age*, Nov 2015, pp. 1–7.

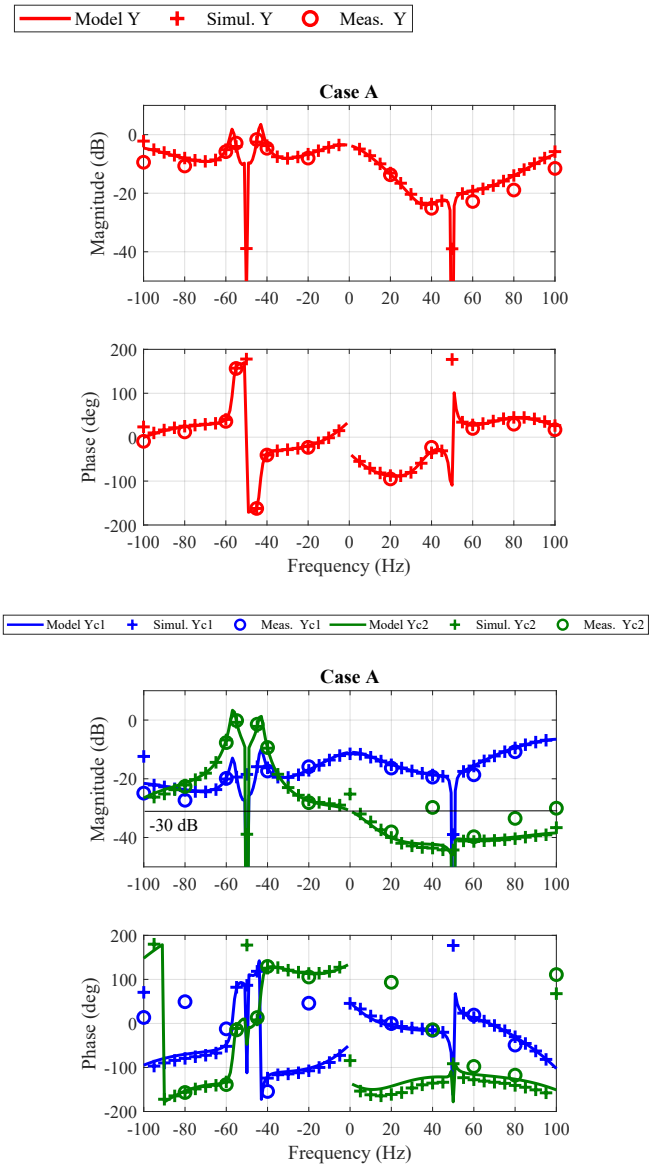

Fig. 27: Validation of analytical model for case A.

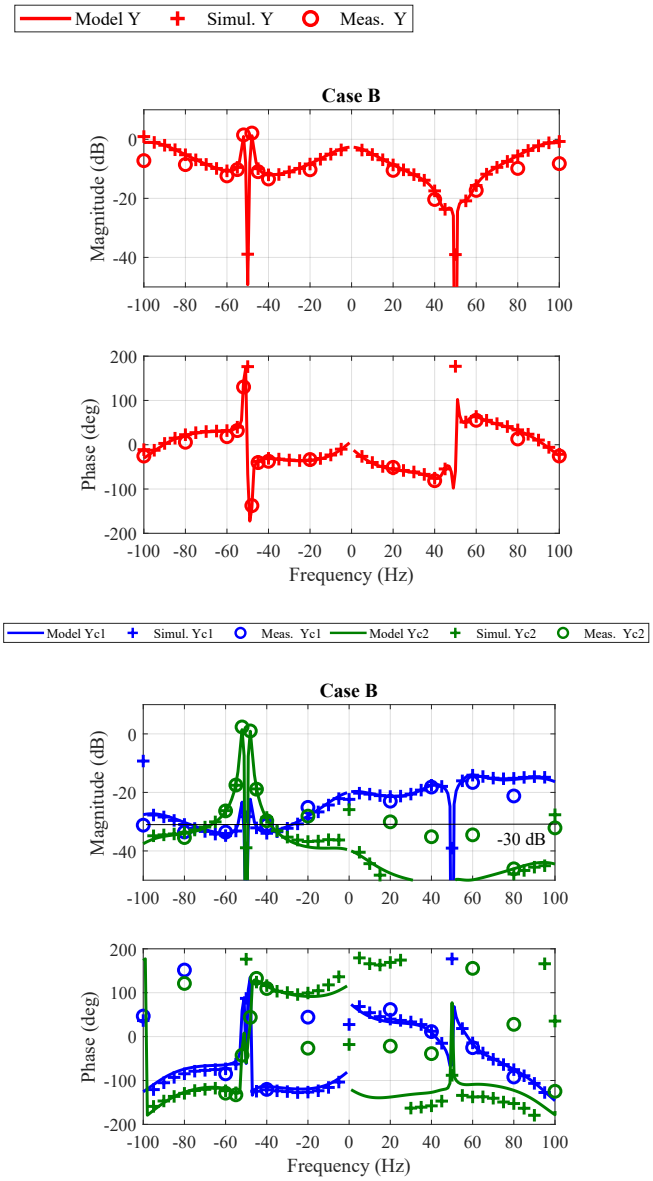

Fig. 28: Validation of analytical model for case B.

[5] C. Li, "Unstable operation of photovoltaic inverter from field experiences," *IEEE Transactions on Power Delivery*, vol. 33, no. 2, pp. 1013–1015, Apr. 2018.

[6] B. Wen, D. Boroyevich, R. Burgos, P. Mattavelli, and Z. Shen, "Analysis of D-Q Small-Signal Impedance of Grid-Tied Inverters," *IEEE Transactions on Power Electronics*, vol. 31, no. 1, pp. 675–687, Jan. 2016.

[7] L. Harnefors, M. Bongiorno, and S. Lundberg, "Input-admittance calculation and shaping for controlled voltage-source converters," *IEEE Transactions on Industrial Electronics*, vol. 54, no. 6, pp. 3323–3334, Dec. 2007.

[8] X. Wang, L. Harnefors, and F. Blaabjerg, "Unified impedance model of grid-connected voltage-source converters," *IEEE Transactions on Power Electronics*, vol. 33, no. 2, pp. 1775–1787, Feb. 2018.

[9] F. D. Freijedo, M. Ferrer, and D. Dujic, "Multivariable high-frequency input-admittance of grid-connected converters: Modeling, validation, and implications on stability," *IEEE Transactions on Industrial Electronics*, vol. 66, no. 8, pp. 6505–6515, 2019.

[10] M. Cespedes and J. Sun, "Impedance modeling and analysis of grid-connected voltage-source converters," *IEEE Transactions on Power Electronics*, vol. 29, no. 3, pp. 1254–1261, Mar. 2014.

[11] A. Rygg, M. Molinas, C. Zhang, and X. Cai, "A modified sequence-domain impedance definition and its equivalence to the dq-domain impedance definition for the stability analysis of AC power electronic systems," *IEEE Journal of Emerging and Selected Topics in Power Electronics*, vol. 4, no. 4, pp. 1383–1396, Dec. 2016.

[12] J. Sun, "Impedance-based stability criterion for grid-connected inverters," *IEEE Transactions on Power Electronics*, vol. 26, no. 11, pp. 3075–3078, Nov. 2011.

[13] C. Zhang, M. Molinas, A. Rygg, and X. Cai, "Impedance-based analysis of interconnected power electronics systems: Impedance network modeling and comparative studies of stability criteria," *IEEE Journal of Emerging and Selected Topics in Power Electronics*, vol. 8, no. 3, pp. 2520–2533, Sep. 2020.

[14] D. Vree, L. Beloqui Larumbe, Z. Qin, P. Bauer, and B. C. Ummels, "Impact of WTG converter impedance model on harmonic amplification factor of the Dutch 110 kV transmission network using a 383 MW wind farm case study," in *CIGRE C4-302*, 2020.

[15] F. D. Freijedo, S. K. Chaudhary, R. Teodorescu, J. M. Guerrero, C. L. Bak, Ł. H. Kocewiak, and C. F. Jensen, "Harmonic resonances in wind power plants: Modeling, analysis and active mitigation methods," in *2015 IEEE Eindhoven PowerTech*, 2015, pp. 1–6.

[16] L. Beloqui Larumbe, Z. Qin, and P. Bauer, "Introduction to the analysis of harmonics and resonances in large offshore wind power plants," in *2018 IEEE 18th International Power Electronics and Motion Control Conference (PEMC)*, Aug. 2018, pp. 393–400.

This article has been accepted for publication in a future issue of this journal, but has not been fully edited. Content may change prior to final publication. Citation information: DOI 10.1109/TPEL.2021.3107045, IEEE Transactions on Power Electronics

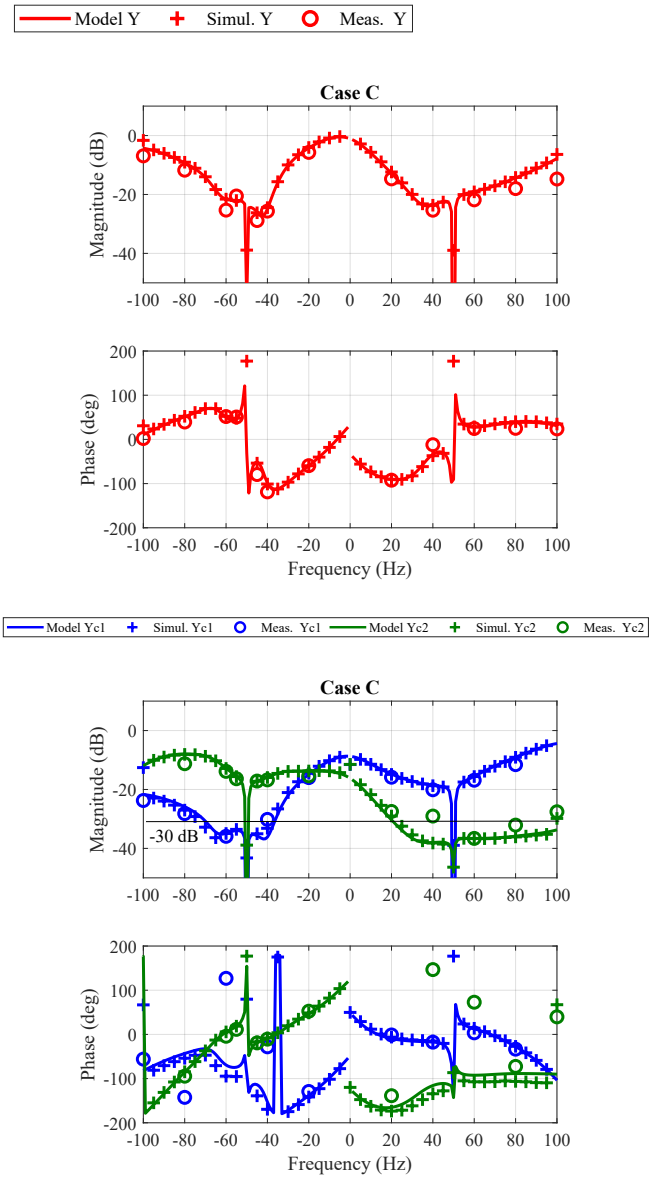

Fig. 29: Validation of analytical model for case C.

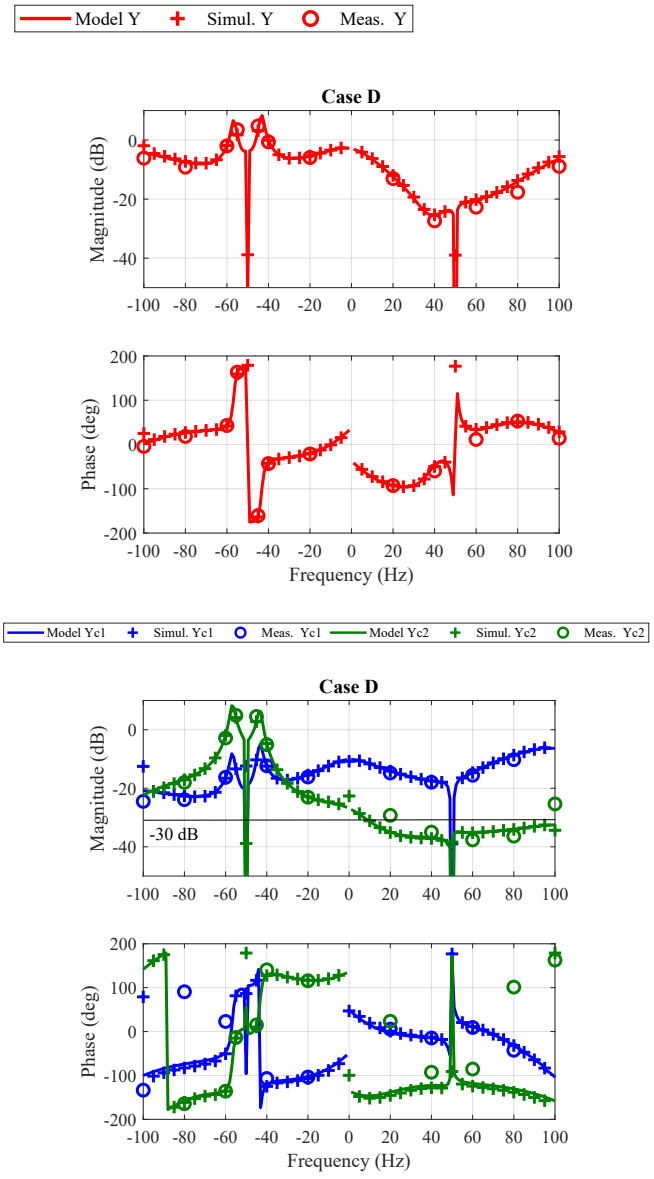

Fig. 30: Validation of analytical model for case D.

[17] Y. Liao, X. Wang, X. Yue, and L. Harnefors, "Complex-valued multi-frequency admittance model of three-phase VSCs in unbalanced grids," *IEEE Journal of Emerging and Selected Topics in Power Electronics*, vol. 8, no. 2, pp. 1934–1946, Jun. 2020.

[18] C. Zhang, M. Molinas, A. Rygg, J. Lyu, and X. Cai, "Harmonic transfer-function-based impedance modeling of a three-phase VSC for asymmetric AC grid stability analysis," *IEEE Transactions on Power Electronics*, vol. 34, no. 12, pp. 12 552–12 566, 2019.

[19] A. Stamatopoulos, H. Vikelgaard, F. F. da Silva, and C. L. Bak, "Power system unbalance due to railway electrification: Review of challenges and outlook of the danish case," in *2016 IEEE International Energy Conference (ENERGYCON)*, 2016, pp. 1–6.

[20] Tsai-Hsiang Chen, "Criteria to Estimate the Voltage Unbalances due to High-Speed Railway Demands," *IEEE Transactions on Power Systems*, vol. 9, no. 3, pp. 1672–1678, Aug. 1994.

[21] A. Bueno, J. M. Aller, J. A. Restrepo, R. Harley, and T. G. Habetler, "Harmonic and Unbalance Compensation Based on Direct Power Control for Electric Railway Systems," *IEEE Transactions on Power Electronics*, vol. 28, no. 12, pp. 5823–5831, Dec. 2013.

[22] A. von Jouanne and B. Banerjee, "Assessment of voltage unbalance," *IEEE Transactions on Power Delivery*, vol. 16, no. 4, pp. 782–790, 2001.

[23] D. Schwanz, F. Möller, S. K. Rönnberg, J. Meyer, and M. H. J. Bollen, "Stochastic Assessment of Voltage Unbalance Due to Single-Phase-Connected Solar Power," *IEEE Transactions on Power Delivery*, vol. 32, no. 2, pp. 852–861, Apr. 2017.

[24] C. F. Flytkjaer, B. Badrzadeh, M. Bollen, Z. Emin, L. Kocewiak, G. Lietz, S. Perera, F. F. Da Silva, and M. Val Escudero, "Power quality trends in the transition to carbon-free electrical energy systems," Cigre Science and Engineering Journal, CSE 017, February 2020.

[25] C. F. Jensen, Ł. H. Kocewiak, and Z. Emin, "Amplification of harmonic background distortion in wind power plants with long high voltage connections," in *CIGRE Biennial Session, CIGRÉ, Paris, France, C4-112*, Aug 2016.

[26] C. H. Ng, L. Ran, and J. Bumby, "Unbalanced-grid-fault ride-through control for a wind turbine inverter," *IEEE Transactions on Industry Applications*, vol. 44, no. 3, pp. 845–856, May 2008.

[27] M. Graungaard Taul, X. Wang, P. Davari, and F. Blaabjerg, "Current reference generation based on next-generation grid code requirements of grid-tied converters during asymmetrical faults," *IEEE Journal of Emerging and Selected Topics in Power Electronics*, vol. 8, no. 4, pp. 3784–3797, Dec. 2020.

[28] X. Wang and F. Blaabjerg, "Harmonic stability in power electronic based power systems: Concept, modeling, and analysis," *IEEE Transactions on Smart Grid*, pp. 1–1, 2018.

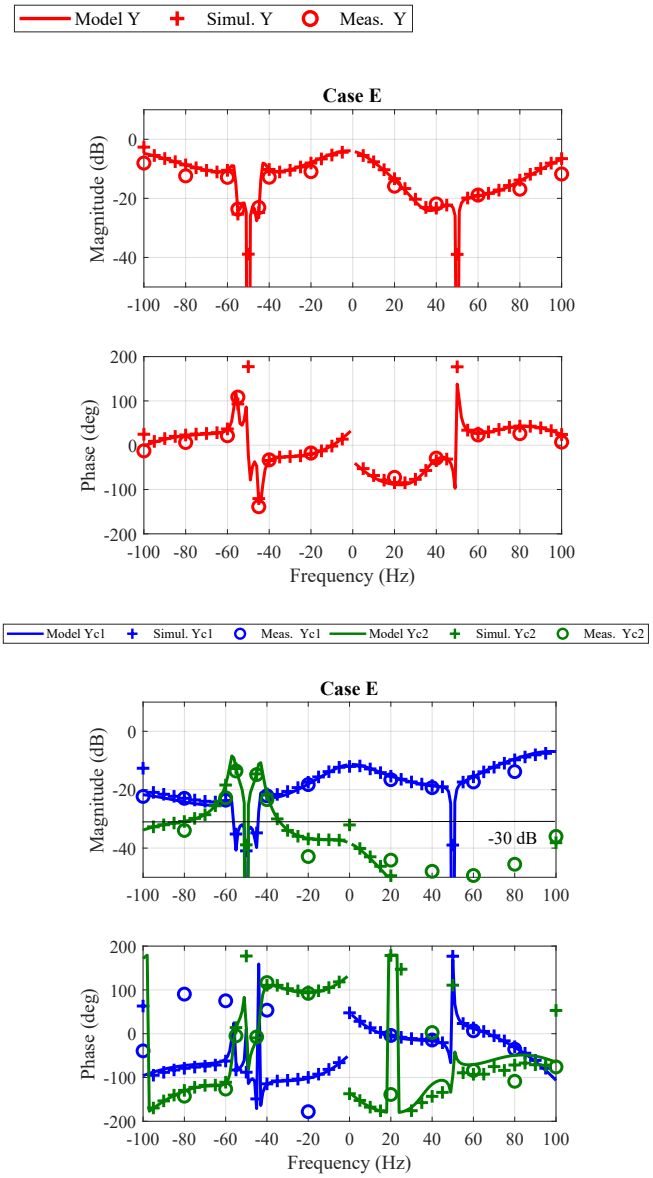

Fig. 31: Validation of analytical model for case E.

[29] L. Harnefors, "Modeling of three-phase dynamic systems using complex transfer functions and transfer matrices," *IEEE Transactions on Industrial Electronics*, vol. 54, no. 4, pp. 2239–2248, Aug. 2007.

[30] M. Reyes, P. Rodriguez, S. Vazquez, A. Luna, R. Teodorescu, and J. M. Carrasco, "Enhanced decoupled double synchronous reference frame current controller for unbalanced grid-voltage conditions," *IEEE Transactions on Power Electronics*, vol. 27, no. 9, pp. 3934–3943, Sep. 2012.

[31] Hong-Seok Song and Kwanghee Nam, "Dual current control scheme for PWM converter under unbalanced input voltage conditions," *IEEE Transactions on Industrial Electronics*, vol. 46, no. 5, pp. 953–959, Oct. 1999.

[32] L. Shuai, R. Sharma, K. H. Jensen, J. N. Nielsen, D. Murcia, S. Pirzada, P. Brogan, and P. Godridge, "Eigenvalue-based stability analysis of subsynchronous oscillation in an offshore wind power plant," in *17th Wind Integration Workshop, Stockholm, Sweden*, Oct 2018.

[33] Ł. H. Kocewiak, J. Hjerrild and C. L. Bak, "Wind turbine converter control interaction with complex wind farm systems," *IET Renewable Power Generation*, vol. 7, no. 4, pp. 380–389, Jul. 2013.

[34] M. Bollen, J. Meyer, H. Amaris, A. M. Blanco, A. Gil de Castro, J. Desmet, M. Klatt, Ł. Kocewiak, S. Rönnberg, and K. Yang, "Future work on harmonics - some expert opinions part i - wind and solar power," in *2014 16th Int. Conf. on Harmonics and Quality of Power*, May 2014, pp. 904–908.

[35] P. Brogan, "The stability of multiple, high power, active front end voltage sourced converters when connected to wind farm collector systems," in *2010 Electrical Power and Energy Conference (EPEC)*, 2010.

[36] L. Beloqui Larumbe, Z. Qin, and P. Bauer, "On the importance of tracking the negative-sequence phase-angle in three-phase inverters with double synchronous reference frame current control," in *29th IEEE International Symposium on Industrial Electronics (ISIE)*, 2019.

[37] S. Golestan, J. M. Guerrero, and J. C. Vasquez, "Three-phase PLLs: A review of recent advances," *IEEE Trans. on Power El.*, no. 3, 2017.

[38] P. Rodriguez, J. Pou, J. Bergas, J. I. Candela, R. P. Burgos, and D. Boroyevich, "Decoupled Double Synchronous Reference Frame PLL for Power Converters Control," *IEEE Transactions on Power Electronics*, vol. 22, no. 2, pp. 584–592, Mar. 2007.

[39] Ł. Kocewiak, "Harmonics in large offshore wind farms," Ph.D. dissertation, Aalborg University, 2012.

[40] L. Beloqui Larumbe, Z. Qin, and P. Bauer, "Output impedance modelling and sensitivity study of grid-feeding inverters with dual current control," in *IECON 2019 - 45th Annual Conf. of the IEEE Ind. El. Soc.*, 2019.

[41] G. Amico, A. Egea-Àlvarez, P. Brogan, and S. Zhang, "Small-signal converter admittance in the *pn*-frame: Systematic derivation and analysis of the cross-coupling terms," *IEEE Transactions on Energy Conversion*, vol. 34, no. 4, pp. 1829–1838, Dec. 2019.

[42] P. B. Brogan, N. Goldenbaum, and J. Thisted, "Wind turbine operation based on a frequency of an AC output voltage signal provided by a power converter of the wind turbine," US Patent US10072633B2, 2015.

[43] H. Wu, X. Wang, K. Wang, G. Li, B. Zhang, and Y. Lu, "Passivity-based harmonic stability analysis of voltage source converters considering the impact of sequence decomposition algorithms," in *2020 IEEE 9th International Power Electronics and Motion Control Conference (IPEMC2020-ECCE Asia)*, Nov. 2020, pp. 1930–1934.

[44] A. Luna, J. Rocabert, J. I. Candela, J. R. Hermoso, R. Teodorescu, F. Blaabjerg, and P. Rodríguez, "Grid voltage synchronization for distributed generation systems under grid fault conditions," *IEEE Transactions on Industry Applications*, vol. 51, no. 4, pp. 3414–3425, Jul. 2015.